International Journal of Plasticity 95 (2017) 163–190

Contents lists available at ScienceDirect

International Journal of Plasticity

journal homepage: www.elsevier.com/locate/ijplas

# Anisotropy, tension-compression asymmetry and texture evolution of a rare-earth-containing magnesium alloy sheet, ZEK100, at different strain rates and temperatures: Experiments and modeling

Saadi A. Habib [a,*], Akhtar S. Khan [a], Thomas Gnäupel-Herold [b], Jeffrey T. Lloyd [c], Scott E. Schoenfeld [c]

[a] Department of Mechanical Engineering, University of Maryland, Baltimore County, MD 21250, USA
[b] NIST Center for Neutron Research, Gaithersburg, MD 20899-8562, USA
[c] Impact Physics Branch, US Army Research Laboratory, Aberdeen Proving Ground, MD, USA

ARTICLE INFO

*Article history:*
Received 14 October 2016
Received in revised form 8 April 2017
Accepted 9 April 2017
Available online 11 April 2017

*Keywords:*
Twinning
Quasi-static
Dynamic
High strain rate
Slip
Crystal plasticity

ABSTRACT

The mechanical response and texture evolution of rare-earth-containing magnesium alloy sheet, ZEK100, are measured under uniaxial (tension and compression) loading along the rolling direction (RD), 45° to rolling direction (DD), transverse direction (TD) and normal direction (ND), at the strain rate of $10^{-4}$ to $3 \times 10^3$ s$^{-1}$, and temperatures of 22 °C & 150 °C. Texture evolution is measured at strain increments between 2 and 10% in compression and tension at both $10^{-4}$ and $3 \times 10^3$ s$^{-1}$, and at 22 °C and 150 °C. Measured pole figures reveal relatively weak basal pole intensity with a spread of basal poles from ND toward TD. Consequently, the yield stress in both tension and compression is the largest in RD and decreases with change in orientation from RD to TD. The material exhibits positive strain rate sensitivity as well as tension-compression asymmetry and anisotropy that are a function of temperature and strain rate. Strain hardening behavior in both tension and compression represents the characteristics of twinning dominated deformation even at elevated temperatures. Crystal reorientation due to extension twinning was observed both in compression along all directions, and in tension along the TD. While the flow stress in compression increases with the increase of strain rate from $10^{-4}$ to $3 \times 10^3$ s$^{-1}$, differences in measured textures between the two strain rates are negligible. A reduced-order crystal plasticity model that defines extension twinning, basal <a> slip, and non-basal slip as the deformation mechanisms, is used to model the experimental results and to give an insight in the active deformation mechanism. The model captures the work hardening, anisotropy and tension-compression asymmetry behavior of the material at different strain rates and temperatures.



* Corresponding author.
*E-mail address:* sahabib1@umbc.edu (S.A. Habib).

http://dx.doi.org/10.1016/j.ijplas.2017.04.006

## 1. Introduction

Due to the rising demand for high strength and lightweight materials, magnesium and its alloys have been at the forefront as possible alternatives to conventional materials such as aluminum and steel. The combination of reasonable mechanical strength and low density is appealing to the transportation industry (Kulekci, 2008), electronics, tools, bio-materials (Staiger et al., 2006), and military applications (Jones et al., 2007). However, in addition to its poor corrosion resistance (Song and Atrens, 1999), magnesium and its alloys typically exhibit poor formability, anisotropy, tension-compression asymmetry, and brittle fracture at room temperature, specifically in its wrought form (Ball and Prangnell, 1994; Lou et al., 2007). These behaviors result in unfavorable mechanical characteristics for manufacturing and design application, therefore hindering its widespread implementation. It is well known that addition of rare-earth elements to magnesium alloys can decrease these unfavorable mechanical characteristics (Rokhlin, 2003). In the past decade, rare-earth-containing magnesium alloys, owing to their promising texture modification, have been of a considerable interest. It is crucial to understand the effects of rare-earth elements on developing favorable characteristics to advance future magnesium alloys. The goal of the present study is to determine the mechanical behavior of a rare-earth-containing magnesium alloy sheet designated as ZEK100 (1.3 %wt. Zn, 0.2 %wt. Nd, 0.25 %wt. Zr and 0.01 %wt. Mn), and to determine the role of the different deformation mechanisms involved in the mechanical behavior and the texture evolution using a reduced-order crystal plasticity model (Becker and Lloyd, 2016).

The poor formability of magnesium can be rationalized by its hexagonal close packed (HCP) crystal structure, which can accommodate a limited number of active slip systems at room temperature. The von Mises criterion (Taylor, 1938; Von Mises, 1928) states a minimum of five independent slip systems are needed for ductile homogeneous deformation of a polycrystalline material. HCP crystal structures can accommodate basal <a> (slip on {0002} plane in $\langle 11\bar{2}0\rangle$ direction), prismatic <a> ($\{10\bar{1}0\}$, $\langle 11\bar{2}0\rangle$), pyramidal <a> ($\{1\bar{1}01\}$, $\langle 11\bar{2}0\rangle$), and pyramidal <c+a> ($\{11\bar{2}2\}$, $\langle 11\bar{2}3\rangle$) slip systems (Groves and Kelly, 1963; Yoo, 1981). These slip systems are activated at different critical resolved shear stresses (CRSS) (Wang and Huang, 2003; Yoo, 1981). At room temperature, the primary slip system of magnesium is on the close packed {0002} plane and thus has a low CRSS (Christian and Mahajan, 1995; Yoo, 1981). Prismatic <a> and pyramidal <a> slip systems are stronger slip modes and require a relatively high CRSS at low temperatures (Agnew et al., 2003; Chapuis and Driver, 2011; Flynn et al., 1961). Combined, basal, prismatic and pyramidal <a> slip can only accommodate four independent systems and none allow for deformation along the c-axis (Yoo, 1981). Furthermore, pyramidal <c+a> slip alone can offer five independent slip modes, however they are difficult to activate at low temperature due to the higher value of CRSS when compared to basal and prismatic <a> slips (Agnew et al., 2001; Yoo et al.,. 2001). Despite the high CRSS for prismatic <a> and pyramidal <c+a> slips, it has been shown that they can play an important role in the ductility of magnesium alloys at low temperatures (Agnew et al., 2001; Koike et al., 2003; Sandlöbes et al., 2011).

Besides the limited dislocation slip activity at room temperature, mechanical twinning is highly active and plays an important role in plastic deformation of magnesium. Mechanical twinning provides an additional deformation mode along the crystallographic c-axis other than pyramidal <c+a> slip (Christian and Mahajan, 1995). Two active twinning mechanisms in magnesium are contraction twinning on the $\{10\bar{1}1\}$ plane in the $\langle 10\bar{1}2\rangle$ direction, and extension twinning on the $\{10\bar{1}2\}$ plane in the $\langle 10\bar{1}1\rangle$ direction (Wonsiewicz, 1966). Contraction twinning provides contraction along the c-axis, as the c-axis is reoriented by 56.2° (Barnett, 2007b; Nave and Barnett, 2004). On the other hand, extension twinning provides elongation along the c-axis from an 86.3° reorientation of the c-axis. Extension twinning in magnesium exhibits a low CRSS value, similar in magnitude to basal <a> slip, and has a significantly lower CRSS value than that for non-basal <a> and <c+a> slips. Therefore, when grains are oriented such that the c-axis undergoes extension, high activity of extension twinning is present (Ardeljan et al., 2016a; Barnett, 2007a; Kelley and Hosford, 1968; Wonsiewicz, 1966). It is important to note that both contraction and extension twinning are polar deformation mechanisms and they can be activated along certain strain paths by direct or indirect extension or contraction of the c-axis (Hong et al., 2010). In addition to extension and contraction twinning, double twinning has also been observed within magnesium on the $\{10\bar{1}1\}$-$\{10\bar{1}2\}$ planes in the $\langle 1\bar{2}10\rangle$ direction (Barnett et al., 2008; Nave and Barnett, 2004; Wonsiewicz, 1966). Double twinning occurs when secondary $\{10\bar{1}2\}$ twinning takes place within the primary $\{10\bar{1}1\}$ twinned volume, producing a 38° rotation from the original crystal matrix orientation. A key signature of high twinning activity is a sigmoidal shaped stress-strain curve (Kabirian et al., 2015; Knezevic et al., 2010; Lou et al., 2007), while it has also been shown that twinning can be active in a parabolic shaped flow stress (Bhattacharyya et al., 2016; Bohlen et al., 2007; Kabirian et al., 2016; Ray and Wilkinson, 2016). It is believed that the initiation, profuse propagation and finally exhaustion of extension twinning within each grain leading to dislocation slip dominated flow is the consequence of the sigmoidal shaped hardening. However, Knezevic et al. (2010) has reported that both contraction and double twinning are also very effective in strain hardening of magnesium alloys by decreasing the mean-free-path of the pyramidal <c+a> dislocations. Although, both contraction and double twinning have been shown to accommodate small to negligible macroscopic strains, and do not contribute to the overall bulk texture measurements (Ardeljan et al., 2016a; Hirsch and Al-Samman, 2013; Jiang et al., 2007).

The limited number of slip systems and the high twinning activity result in unfavorable mechanical characteristics. During the manufacturing processes, the material develops a strong crystallographic texture with the c-axis normal to the die surface. Consequently, wrought magnesium alloys exhibit both tension-compression asymmetry as well as anisotropy (Jain and Agnew, 2007; Lou et al., 2007) which has also been seen in other HCP materials (Meredith and Khan, 2012; Tenckhoff, 2005). These factors add complexity for design applications, as the material properties are directional and require advanced modeling; thus, these factors can limit the use of magnesium alloys in commercial application. The mechanical properties of wrought magnesium can be improved by texture modification and grain size reduction, e.g. through processes such as equal channel angular pressing (ECAP) (Barnett et al., 2004) and the spinning water atomization process (SWAP) (Kondoh et al., 2010). Many authors have reported that grain refinement and texture modification are effective methods in improving ductility of magnesium due to the activation of non-basal slip (Atwell et al., 2012; Barnett et al., 2004; Jain et al., 2008; Koike et al., 2003; Meredith et al., 2016; Raeisinia and Agnew, 2010). Recently, Ardeljan et al. (2016b) showed that in case of nano-layered Zr/Nb composites, the ductility and specific texture development arise from substantially reduced ratio of slip resistance among basal and non-basal slip systems. This has been also shown in ECAP processed AZ31 by Kabirian et al. (2016), where extension twinning, basal and non-basal slips approaches similar relative activities as the grain size and texture intensity decreased with each additional ECAP pass. Nonetheless, processes such as ECAP and SWAP are typically limited to extruded materials, require additional manufacturing resources, and are not cost-effective.

Alloying magnesium with rare-earth elements, such as cerium (Ce), neodymium (Nd), lanthanum (La), yttrium (Y) and gadolinium (Gd), have been shown to reduce the strong crystallographic texture of magnesium (Al-Samman and Li, 2011; Bohlen et al., 2007; Chino et al., 2008; Rokhlin, 2003). The commercially available non-rare-earth-containing magnesium alloy AZ31 (sheet) exhibits the maximum basal pole intensity in and around the sheet normal direction with a wider basal spread towards the rolling direction (Khan et al., 2011). On the other hand, Bohlen et al. (2007) have studied the effect of rare-earth-containing magnesium alloys and have concluded that the maximum basal pole intensity is located $\pm 20^{\circ}$ from the sheet normal direction towards rolling direction with a broad basal pole spread from the normal direction towards the transverse direction, and hence a lower maximum intensity compared to AZ31. However, other authors have reported that the maximum basal pole intensity and the wide spread of basal poles are located from the normal direction towards the transverse direction (Al-Samman and Li, 2011; Mackenzie and Pekguleryuz, 2008). Nonetheless, small percent of rare-earth elements results in a weaker crystallographic texture, and therefore, an increase in formability and a reduction in tension-compression asymmetry. Mishra et al. (2008) have experimented with a magnesium alloy with 0.2 wt% Ce and compared it to pure magnesium. The study concluded that an increase in ductility was possible not only due to the weaker texture, but also from grain refinement. Correspondingly, the weak texture and reduced grain size are dependent on the rolling temperature, rolling thickness reduction, and other alloying elements (Bohlen et al., 2007; Mackenzie and Pekguleryuz, 2008; Wendt et al., 2009). Basu and Al-Samman (2014) showed an improvement in ductility and grain refinement of rare-earth-containing magnesium alloys with the addition of zinc and zirconium, from the increase in activity of non-basal slip. Furthermore, the weakening of the crystallographic texture of rare-earth-containing magnesium alloys has been linked to static and dynamic recrystallization processes (Basu et al., 2013; Basu and Al-Samman, 2014, 2015; Bohlen et al., 2007; Drouven et al., 2015; Hadorn et al., 2012, 2013; Hantzsche et al., 2010; Jung et al., 2015; Mackenzie and Pekguleryuz, 2008; Senn and Agnew, 2008; Stanford and Barnett, 2008; Wendt et al., 2009). It has been also observed that a change in stacking fault energy as a result of rare-earth alloying can be associated with the improvement in ductility by the enhancement of non-basal slip (Chino et al., 2008; Sandlöbes et al., 2011, 2012). Despite the decrease in texture intensity due to addition of rare-earths and other constituents, a difference in distribution of the basal poles from one axis to another, results in strong anisotropic properties, specifically at low temperatures.

The Lankford coefficient/plastic strain ratio (r-value) is an important parameter used to measure the anisotropy of rolled materials. A variation in the r-value with respect to orientation in the plane of the sheet is unfavorable because it signifies high anisotropy and results in problems such as "earing". Typically, a high r-value translates to better resistance to sheet thinning, therefore maintaining adequate sheet thickness throughout a large strain forming process (Hosford and Caddell, 2011). However, it has been shown that a high r-value for magnesium alloys results in poor formability at room temperature, and that other material properties can play an important role in the formability (Agnew and Duygulu, 2005; Boba et al., 2015; Bohlen et al., 2007; Kurukuri et al., 2014). Not only are the r-value parameters important in understanding the anisotropic behavior for forming processes, they are also important in understanding the activity of different deformation mechanisms. For example, when the basal pole intensity is in the normal direction, for AZ31 sheet, one of the main deformation mechanisms during in-plane tension is prismatic <a> slip resulting in greater strain in the width than the thickness direction and thus an r-value greater than 1 (Agnew and Duygulu, 2005; Atwell et al., 2012; Jain and Agnew, 2007). On the contrary, it has been reported that the r-value typically increases as the plastic strain increases, and decreases as the strain rate increases in tension, which can be attributed to the contribution of different deformation mechanism (Khan et al., 2011; Lou et al., 2007). Alternatively, the r-value in compression for AZ31 is less than 1 due to the high activity of extension twinning (Jain and Agnew, 2007). The authors also showed that an increase in r-value in compression at temperatures of 175 °C–250 °C is from the increase in non-basal slip as the temperature increases (Jain and Agnew, 2007). Comparably, ZEK100 sheet also showed an evolving r-value as plastic strain increases (Kurukuri et al., 2014; Muhammad et al., 2015; Steglich et al., 2014). However, ZEK100 exhibits an r-value less than 1 in all directions in both tension and compression at room temperature. Other than the r-value at room temperature, no experimental results are published for both elevated temperatures and high strain rates for rare-earth-containing magnesium alloys. Furthermore, no comparisons regarding the r-value and crystallographic texture evolution have been made specifically for the unique texture of ZEK100. These comparisons can play an important role in understanding the effects of the weaker texture on the deformation mechanisms.

Besides the r-value, strain rate sensitivity is a critical factor in a successful metal forming process where a positive strain rate sensitivity helps in stable plastic flow (Ghosh, 1977). Additionally, to evaluate crashworthiness of a material for transportation and defense industries, high strain rate experiments are carried out in order to create a material model for simulation of deformation during crash and impact. Thus, the strain rate sensitivity of a material plays a vital role in design applications where strength and ductility are assessed as a function of strain rate. Regarding effects of strain rate on mechanical properties of magnesium alloys, many studies have focused on dynamic loading on conventional magnesium alloys (Pandey et al., 2015; Prasad et al., 2014; Tucker et al., 2009; Ulacia et al., 2010). The consensus is that magnesium alloys exhibit positive strain rate sensitivity in tension and compression specifically at elevated temperatures. Alternatively, experimental data at high strain rates on a rare-earth-containing magnesium alloy are limited to room temperature (Agnew et al., 2014; Bhattacharyya et al., 2016; Kurukuri et al., 2014). Kurukuri et al. (2014) recently showed an increase in compressive flow stress as strain rate increases from the quasi-static to the dynamic regime along all directions for ZEK100 sheet. Moreover, as a result of the wide distribution of basal poles in the transverse direction, no tension-compression asymmetry of the yield strength is present even at high strain rates. While there are experimental data at room temperature, high temperature data at low and high strain rates are scarce. Furthermore, there is great interest regarding texture evolution as a function of strain rate. Kabirian et al. (2015) evaluated, for AZ31, the increase in flow stress as the strain rate increases by texture measurements at specific percent strain at different strain rates. They concluded that as the strain rate increases from quasi-static to dynamic, there is an accelerated twinning activity and an increase in rate sensitivity of active slip systems. Comparatively, no published data for rare-earth-containing magnesium alloys regarding texture evolution at different strain levels for both quasi-static and dynamic loadings, and different temperatures is present.

The objective of this study is to present a comprehensive understanding of the mechanical response at quasi-static and dynamic strain rates, and at different temperatures under uniaxial loading (tension and compression) for ZEK100. Even though there are published experimental results on ZEK100, the literature lacks comprehensive mechanical stress-strain data, r-value and results on strain rate sensitivity at different strain rates, temperatures and loading directions. In addition, the literature lacks studies of the texture evolution at different levels of plastic strain, different strain rates and temperatures for ZEK100. Lastly, a reduced-order crystal plasticity model developed by Becker and Lloyd (2016) will be implemented in order to determine the role of the deformation mechanisms involved in the mechanical behavior and the texture evolution.

## 2. Experimental procedure

### 2.1. Material

A rolled 1.6 mm thick rare-earth-containing magnesium alloy sheet, ZEK100 (1.3 %wt. Zn, 0.2 %wt. Nd, 0.25 %wt. Zr and 0.01 %wt. Mn) was used in this study in an as-fabricated condition. An initial micrograph image was prepared by polishing and etching in an acetic picral solution (4.2 g picric acid, 10 ml acetic acid, 70 ml ethanol and 10 ml distilled water).

### 2.2. Quasi-static tension and compression experiments

The ZEK100 sheet was subjected to mechanical experiments in compression and tension at quasi-static loading using a MTS-809 axial/torsional servo-hydraulic system at strain rates of $10^{-4}$, $10^{-2}$, and $10^{0}$ $s^{-1}$, and at temperatures of 22 °C and 150 °C. Dog-bone-shaped tension specimens were prepared along the rolling direction (RD), 45° to rolling direction (DD), and transverse direction (TD), as shown in Fig. 1. Gage length and width of the tension specimens were 31.0 mm and 6.4 mm,

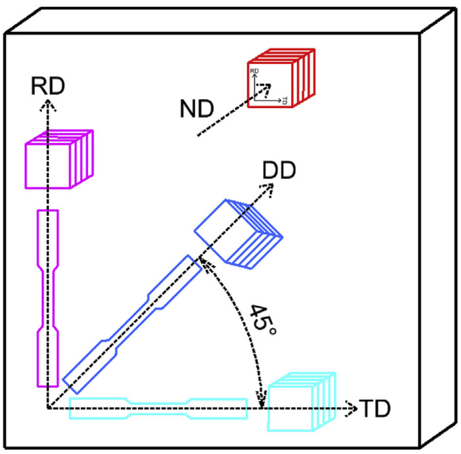


**Fig. 1.** Schematic of compression and tension specimens in rolling (RD), diagonal (DD), transverse (TD) and normal direction (ND) (not to scale).

respectively. The displacement data in tension at 22 °C was corrected by using a high elongation Kyowa strain gage (KFEL-2-120-C1) on the specimen. The quasi-static compression specimens were prepared along the RD, DD, TD and the thickness or normal direction (ND) by bonding four sheets using J-B Weld® adhesive. Each sheet was lightly sanded with 240-grit and precaution was taken when sanding to avoid any through thickness variation prior to bonding. Pressure was maintained after bonding with special parallel clamps to avoid any variation in clamping pressure and successfully eliminating any irregularity in the final thickness of the stacked-up specimen after curing. The compression RD, DD and TD specimens were machined to the gage length of 5.9 mm and a square cross sectional area of 37.8 $mm^2$, and the ND specimen was machined with a gage length of 6.1 mm and a square cross sectional area of 37.8 $mm^2$. The displacement data in compression were corrected using a "blank test" which provided compliance of the machine, platens, and lubrication. The specimen contact surfaces were polished with a final sand paper grit of 1200 and lubricated using Dow Corning® high vacuum grease and M.K. Impex Canada mk-ws2-ht high temperature tungsten disulfide grease to reduce friction and maintain a uniform stress state for experiments performed at 22 °C and 150 °C, respectively. High temperature experiments were performed using a custom convection furnace resulting in faster heating time and temperature homogeneity throughout the gage length of the specimen when compared to conventional split electric furnace. All 150 °C experiments were temperature-controlled using a thermocouple cemented directly on the sample surface.

### *2.3. Dynamic tension and compression experiments*

The split-Hopkinson pressure bar technique (SHPB) was utilized to perform dynamic uniaxial compression and tension experiments at a nominal engineering strain rate of approximately $3 \times 10^3\ s^{-1}$ and $6 \times 10^2\ s^{-1}$, respectively, as shown in Fig. 2. Dog-bone-shaped tension specimens were prepared for the RD, DD, and TD. The tension specimens were machined with 12.5 mm gage length, a gage width of 1.9 mm, and thickness of 1.5 mm (sheet thickness). Dynamic compression specimens were prepared for the RD, DD, TD and ND by bonding multiple sheets using J-B Weld® adhesive, similar to quasi-static compression procedure. The compression samples were machined with a gage length of 3.3 mm and with a square cross sectional area of 37.8 $mm^2$ for the RD, DD, and TD samples, while the ND samples were prepared with a gage length of 2.8 mm and square cross sectional area of 37.8 $mm^2$.

Sample geometry is important when performing experiments at high strain rate. The sample geometry is designed to reduce the longitudinal and radial inertia effects on the deformation behavior (Khan and Liang, 1999). For dynamic compression experiments, Khan and Liang (1999) showed the optimum length to diameter (L/D) ratio is between 0.2 and 0.5. Khan et al. also performed experiments with samples with different L/D ratio and reported no significant differences between L/D ratios of 0.2–0.5 for different materials (Khan and Liang, 1999; Khan and Farrokh, 2006). In a split-Hopkinson pressure bar experiment, deformation takes place due to travelling stress waves. For the stress-strain equation using the incident, reflected

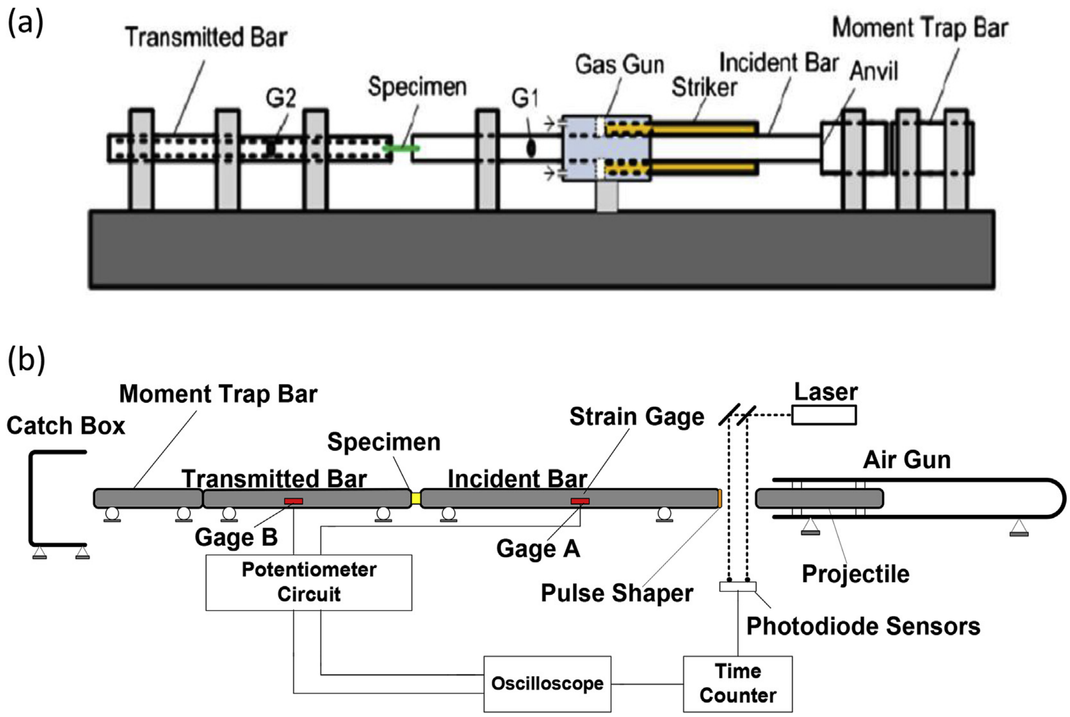


**Fig. 2.** Tension (a) and compression (b) split hopkinson pressure bar (SHPB).

and transmitted waves to be valid, equilibrium of the stress throughout the test sample must be reached. This requires several reverberations of the stress wave through the sample to achieve uniform deformation and for the wave analysis to be valid. Consequently, the length of the sample plays an important role in the time duration and subsequently time to reach the stress equilibrium. The dimensions of the dynamic compression samples in the present study falls into an L/D ratio between the accepted values and the shorter length resulting in reaching stress equilibrium within an acceptable duration. The dynamic tension specimen dimensions were also designed to have smaller dimensions than that of quasi-static strain rates to reach stress equilibrium quickly. Smerd (2005) showed that tension specimens with a gage length of 12.5 mm and a gage width of 1.75 mm exhibited similar stress–strain response to that of an ASTM-E8 (2004) sub size standard with a 25 mm gage length during uniform elongation. Ulacia et al. (2011) also reported similar comparison on magnesium alloy AZ31. Because of the difference in the geometry of the dynamic and quasi-static tension specimens, the reader should be cautious when comparing the quasi-static and dynamic experimental results during post uniform elongation. This is specifically true for tensile loading in the RD, as tensile loading in the TD and DD does not exhibit post necking elongation due to the duration and magnitude of the incident wave.

Two strain gages at diametrically opposing locations on both, the incident and the transmitted bars, connected in a potentiometer circuit, were used to cancel any bending effects for both tension and compression SHPB. The strain-time histories for incident, transmitted and reflected waves were recorded using a Nicolet 440 oscilloscope. An annealed copper C110 “pulse shaper” of 4 mm diameter and 0.25 mm thickness was used to dampen undesirable oscillation of the compressive incident wave. A description of the direct tension SHPB is provided in Khan et al. (2010) and compression SHPB is provided in Khan and Liang (1999). High temperature dynamic compression and dynamic tension experiments were performed using small convection furnace and heating tape, respectively. The area adjacent to the heated area of the bars was cooled to prevent any temperature effects on the waves. For probing the texture evolution at different intermediate strains for dynamic compression experiments, ring spacers with specific thickness around the specimen were used to interrupt the experiment at a particular strain similar to Huskins et al. (2010) and Kabirian et al. (2015).

### 2.4. Plastic anisotropy

The Lankford coefficient (r-value) was used to measure plastic anisotropy. By convention, r-value measurements are performed at an intermediate strain or up to uniform elongation. However, magnesium alloys typically exhibit an r-value that evolves with increasing plastic deformation as a result of evolving crystallographic texture (Andar et al., 2012; Lou et al., 2007). Some authors have reported diffuse necking within magnesium alloys (Atwell et al., 2012; Kang et al., 2013; Muhammad et al., 2015). Kang et al. (2013) used digital image correlation to measure the r-value post necking and suggested that the r-value should be measured at a single point rather than over the entire gage length because of both inhomogeneous deformation and diffuse necking that is present during deformation. Therefore, in this study, the r-value was measured at different locations before and after necking. The experiments for the r-value measurement in tension were conducted as a sequence of loading and then unloading. Subsequently, the length, width and thickness were measured at four different marked locations within the gage section using a digital micrometer and caliper. The resulting strain in the width, thickness and gage length was calculated. Assuming isochoric deformation (no volume change), the axial strain at each of the four locations was calculated using strains in the width and thickness directions, and compared to measured axial strain to validate the accuracy of the measurements.

The cumulative r-value in tension was calculated as:

$$r_{Tensile} = \frac{\varepsilon_w^{pl}}{\varepsilon_t^{pl}} \tag{1}$$

where $\varepsilon_w^{pl}$ and $\varepsilon_t^{pl}$ are true plastic strain in the width and thickness, respectively. The calculated and measured gage length axial strain and the r-value at four different locations should be the same up to necking within the accuracy of the measurement tool. After necking both the calculated and measured gage length strain and the r-value at four different locations starts to vary due to non-uniform elongation throughout the gage section. However, it should be noted that as the post necking elongation becomes non-uniform across the gage length, the strain rate within the necking region increases accompanied by a commensurate decrease in strain rate outside the necking region. This method works well for ZEK100 since the through-thickness strain is large enough to be measured with a digital micrometer (Accuracy of ±0.001 mm). The same sample was then reloaded to the subsequent plastic strain and the procedure was applied again.

Similarly, the r-value in compression was calculated using measurements of the length and width for the RD, DD and TD. The cumulative r-value in compression was calculated as:

$$r_{Compressive} = \frac{\varepsilon_w^{pl}}{-\left(\varepsilon_l^{pl} + \varepsilon_w^{pl}\right)} \tag{2}$$

where $\varepsilon_w^{pl}$ and $\varepsilon_l^{pl}$ are true plastic strain in the width and length, respectively.

### 2.5. Texture measurements

Neutron diffraction texture measurements were performed at the Center of Neutron Research, National Institute of Standard and Technology (NIST), Maryland, USA. A description of the texture measurement technique is given in Khan et al. (2011). Using the MTEX algorithm developed by Hielscher and Schaeben (2008), the orientation distribution function (ODF) was calculated using five ($\{0002\}, \{10\overline{1}0\}, \{10\overline{1}1\}, \{11\overline{2}2\}$, and $\{20\overline{2}1\}$) and three ($\{0002\}, \{10\overline{1}0\}$, and $\{10\overline{1}1\}$) measured poles for compression and tension, respectively, which was then used to recalculate the pole figures.

## 3. Modeling

Details of the reduced-order, crystallographic constitutive model used in this work are presented elsewhere (Becker and Lloyd, 2016), and has been shown to reproduce the mechanical behavior of magnesium alloys AZ31B and AMX602 (Becker and Lloyd, 2016; Meredith et al., 2016). The model employs the following assumptions for computational efficiency and numerical robustness: twinning is crystallographic but reorientation effects are not included; basal slip is crystallographic but approximated as a single aggregate slip system that acts in the direction of maximum resolved shear stress in the basal plane, denoted $\widehat{\mathrm{s}}_{\mathrm{bas}}$; and the combination of prismatic <a> and pyramidal <c+a> slip are aggregated into a single, isotropic deformation mechanism (Becker and Lloyd, 2016; Lloyd and Becker, 2016; Meredith et al., 2016), denoted $\varepsilon_{\mathrm{nb}}$, and hereafter referred to as “non-basal slip”. It should be noted that the inclusion of a rate and temperature dependent isotropic deformation component within a plasticity framework has been used in literature as well (Khan et al., 2015; Knezevic et al., 2013; Staroselsky and Anand, 2003). The velocity gradient associated with these approximations is given as:

$$\mathbf{L}^P = \sum\nolimits_{\alpha=1}^{6} \dot{\gamma}^{\alpha}_{\mathrm{twin}} \left(\mathbf{s}^{\alpha}_{\mathrm{twin}} \otimes \mathbf{m}^{\alpha}_{\mathrm{twin}}\right) + \dot{\gamma}_{\mathrm{bas}} \left(\widehat{\mathbf{s}}_{\mathrm{bas}} \otimes \mathbf{m}_{\mathrm{bas}}\right) + \dot{\varepsilon}_{\mathrm{nb}} \frac{3\boldsymbol{\sigma}'}{2\sigma_{vm}} \tag{3}$$

As in prior works, basal <a> slip and twinning are assumed to be rate-independent, and modeled using Voce and linear hardening, respectively

$$\tau_{bas} = \tau_{0,\mathrm{bas}} + \tau^{\infty}_{\mathrm{bas}} \left[1 - \exp\left(\frac{-h_{\mathrm{bas}} \gamma_{\mathrm{bas}}}{\tau^{\infty}_{\mathrm{bas}}}\right)\right] \tag{4}$$

$$\tau^{\alpha}_{\mathrm{twin}} = \tau_{0,\mathrm{twin}} + h_{\mathrm{twin}} \gamma^{\mathrm{tot}}_{\mathrm{twin}} \tag{5}$$

where $\tau_{bas}$ and $\tau^{\alpha}_{\mathrm{twin}}$ are the flow strengths for basal slip and twinning, respectively, and other terms are material parameters. It is well known that pyramidal-prismatic components of the deformation are temperature and strain rate dependent (Akhtar, 1975; Akhtar and Teghtsoonian, 1969b; Bhattacharyya et al., 2016; Flynn et al., 1961; Ulacia et al., 2010). Therefore, the hardening law for non-basal slip can be modeled using traditional isotropic constitutive hardening models such as Johnson and Cook (1983) and Zerilli and Armstrong (1987). As discussed later sections, tension in the RD is predominantly deformed by non-basal slip and thus, the tension results in RD are used to model the strength and hardening behavior of non-basal slip. However, both the Johnson-Cook and Zerilli-Armstrong models are unable to model the RD tension response at different temperatures and strain rates with a single set of constants.

The KHL model proposed by Khan and Liang (1999) has been subjected to many modifications over the years. Recently Kabirian et al. (2014) has modified and incorporated a rate insensitivity term to incorporate negative rate sensitivity of aluminum alloy, 5182-O, sheet up to a threshold strain rate and threshold temperature with great success. Consequently, to accommodate the thermo-mechanical response of ZEK100, similar form of the Kabirian et al. (2014) model is utilized to model the increase in strain rate sensitivity as the temperature increases and capture the decrease in flow stress at elevated temperatures. To rationalize this difference in flow stress, the negative strain rate sensitivity term in Kabirian et al. (2014), $\varphi(\dot{\bar{\varepsilon}}_p, T)/(1 + |\varphi(\dot{\bar{\varepsilon}}_p, T)|)$, was set to one. With the negative strain rate sensitivity term set to one, the model correlated to the experimental data successfully; however, the $\exp(C_1 \dot{\varepsilon}_{\mathrm{nb}}/\dot{\varepsilon}^*)$ term results in very high stress and divergence of the data at very high strain rates. By replacing the exponential rate dependent term with a logistic function, the data converges as the strain rate is increased. The following equation is capable of predicting the rate and temperature dependent flow stress of ZEK100 during deformation mode that is mediated by non-basal slip:

$$\begin{aligned}\sigma_{vm} = &\left[A + F\gamma^{\mathrm{tot}}_{\mathrm{twin}} + B\varepsilon^{n_o}_{nb}\left(1 - \frac{\ln(\dot{\varepsilon}_{\mathrm{nb}}/\dot{\varepsilon}^*)}{\ln(D_p)}\right)^{n_1}\left(\frac{T_m - T}{T_m - T_r}\right)^{m_3}\right]\left[\left(\frac{C}{1 + \exp\left(-C_1\sqrt{\dot{\varepsilon}_{\mathrm{nb}}/\dot{\varepsilon}^*}\right)}\right)^{n_2}\right. \\ &\left. - D\exp(-K\dot{\varepsilon}_{\mathrm{nb}})\left(\frac{T}{T_m}\right)^{m_1}\right]\left(\frac{T_m - T}{T_m - T_r}\right)^{m_2}\end{aligned} \tag{6}$$

where $\sigma_{vm}$, $\varepsilon_{nb}$ and $\dot{\varepsilon}_{nb}$ are the flow stress, the current plastic strain and the current plastic strain rate of non-basal slip, respectively. $T$, $T_{\mathrm{m}}$ and $T_{\mathrm{r}}$ are the current, melting and reference temperature, respectively. $D_{\mathrm{p}}$ is an arbitrary maximum strain rate and $\dot{\varepsilon}^{*}$ is the reference strain rate at which the strain rate effect term reduces to unity. Other terms not discussed are material parameters. It is important to note, once Eq. (6) is correlated to the tension loading in the RD to determine material constants, the material parameters in Eq. (6) remain unchanged, other than the constant F, during the modeling of basal <a> slip and extension twinning.

Even if the $n_2$ exponent is set to one, the correlation of the model and experimental results are reasonable. However, the $n_2$ exponent allows for modeling specific material response at high strain rates. The specific values of material constants for ZEK100 are included in Table 1. One representative set of material constants was used for all correlations and predictions. In order to better visualize the stress during the deformation mode that is mediated by non-basal slip, a plot is shown in Fig. 3, describing the Von Mises equivalent stress for non-basal slip, as a function of strain rate at 22 °C and 150 °C and at strains of 0% and 5% when total twinning shear strain is zero.

The model was implemented as a local Abaqus UMAT. The simulations contained approximately 300 grains and 1400 fully integrated hexahedral elements (C3D8). Representative polycrystalline microstructures were instantiated using a voxelated Voronoi tessellation, where grain orientations were sampled based on the experimentally measured pole figures.

## 4. Results and discussion

### 4.1. Initial micrograph and crystallographic texture

The microstructure of the as-received ZEK100 sheet is shown in Fig. 4. The grain structure consists of noticeable large grains and smaller recrystallized grains. Several grains contain partially twinned regions as a result of the plastic deformation during the rolling process and the absence of full recrystallization. Fig. 5 shows the as-received (0002) and $(10\bar{1}0)$ pole figure and the average intensity in multiples of random distribution (mrd) from the basal texture as a function of tilt angle from the ND in both the RD and TD. The maximum basal fiber texture are aligned $\pm$35–40° tilt from the ND to the TD at 3.26 mrd with a wide spread of basal pole in the TD from the ND. The prismatic pole intensity is highly aligned in the RD without a 6-fold symmetry about the ND, due to the wide spread of basal poles in the TD from the ND.

### 4.2. Effects of the loading direction on the mechanical behavior

#### 4.2.1. Yield stress, flow behavior and strain rate sensitivity

Figs. 6–9 shows the mechanical response of ZEK100 under uniaxial tension and compression at 22 °C and 150 °C, and at different strain rates for the RD, DD, TD and ND. The related mechanical properties for the RD, DD, TD and ND are summarized in Table 2. It should be noted that even though the 0.2% yield stress at dynamic strain rates was measured, the yield stress is an approximation since equilibrium of stress throughout the test sample requires several reverberations of the stress waves to achieve uniform deformation and for the wave analysis to be valid. Nonetheless, the tensile response of ZEK100 exhibits stronger yield anisotropy than the conventional magnesium alloy AZ31 (Khan et al., 2011). The tensile yield strength is the

**Table 1**
Material parameters used for the reduced-order crystal model of ZEK100.

| Parameter | Value | Units |
|---|---|---|
| $\tau_{0,\mathrm{bas}}$ | 40 | MPa |
| $\tau_{\mathrm{bas}}^{\infty}$ | 10 | MPa |
| $h_{\mathrm{bas}}$ | 5*10$^3$ | MPa |
| $\tau_{0,\mathrm{twin}}$ | 30 | MPa |
| $h_{\mathrm{twin}}$ | 10 | MPa |
| $A$ | 239 | MPa |
| $B$ | 175 | MPa |
| $C$ | 2 | – |
| $C_1$ | 8*10$^{-3}$ | – |
| $D$ | 2.75 | – |
| $F$ | 750 | MPa |
| $K$ | 60 | s |
| $\dot{\varepsilon}^{*}$ | 1 | s$^{-1}$ |
| $D_{\mathrm{p}}$ | 10$^9$ | s$^{-1}$ |
| $m_1$ | 2.7 | – |
| $m_2 = m_3$ | 1 | – |
| $n_o$ | 0.33 | – |
| $n_1$ | −0.37 | – |
| $n_2$ | 1.3 | – |
| $T_r$ | 295 | K |
| $T_m$ | 873 | K |

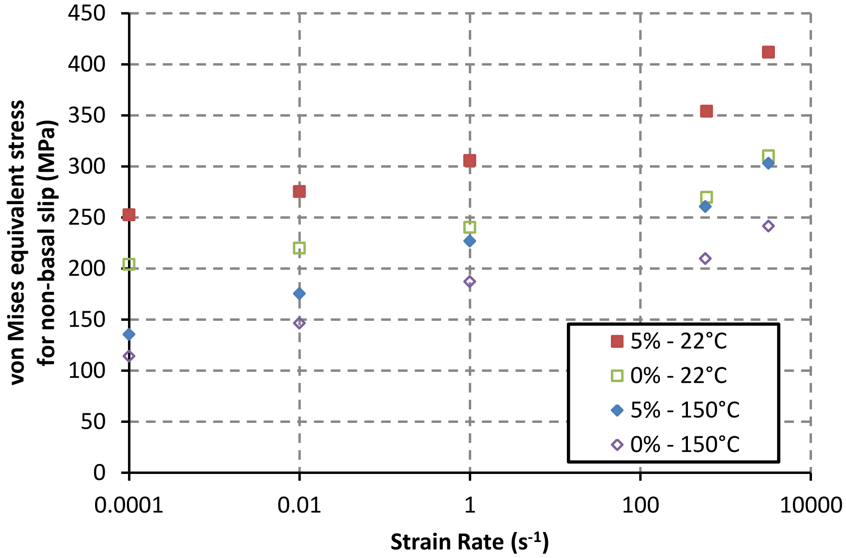


**Fig. 3.** Von Mises equivalent stress for non-basal slip as a function of strain rate at 22 °C and 150 °C and at 0% and 5% plastic strain when total twinning shear strain is zero.

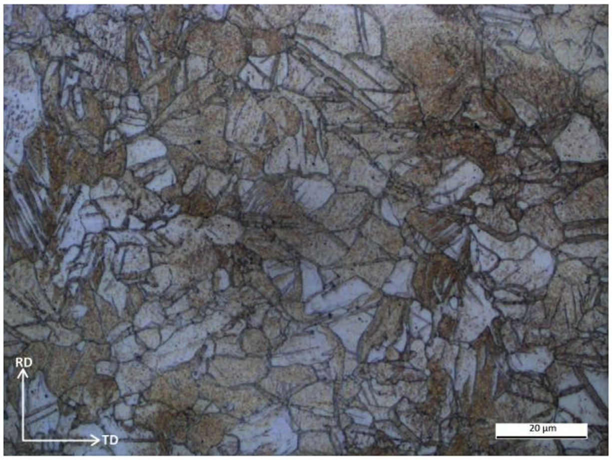


**Fig. 4.** Optical micrograph of magnesium alloy sheet, ZEK100.

largest in the RD and decreases with a change in loading direction to the TD. The anisotropic response is due to the different active deformation mechanisms, specifically the wide spread of the basal pole intensity in the TD from the ND, which will be discussed in detail within Section 4.3–4.4. The stress-strain curves in tension in the RD (Fig. 6) display positive strain rate sensitivity during plastic yielding at both temperatures, resembling the characteristic of rate dependent dislocation slip activity, similar to BCC materials. Unlike tension loading in the RD, it was observed that the tensile yield stress in the DD and TD at 22 °C was strain rate insensitive during the quasi-static loading with slight (~10–15 MPa, though it is an approximation) differences from quasi-static to dynamic loading. The yield strength rate insensitivity is a characteristic of rate independent basal <a> slip and extension twinning. While the tensile yield stress is strain rate insensitive in the DD and TD at 22 °C, increasing the temperature to 150 °C results in positive strain rate sensitivity.

The strain hardening response in tension along all direction, and at both temperatures is parabolic. To characterize hardening response, strain-hardening exponent was defined using the power law relationship (Hollomon, 1945):

$$\sigma = k\varepsilon_p^n \tag{7}$$

where the k is the strength coefficient, n is the strain-hardening exponent and $\varepsilon_p$ is the true plastic strain up to uniform elongation. Clearly, as the strain hardening of the material increases, the strain-hardening exponent also increases. The strain-

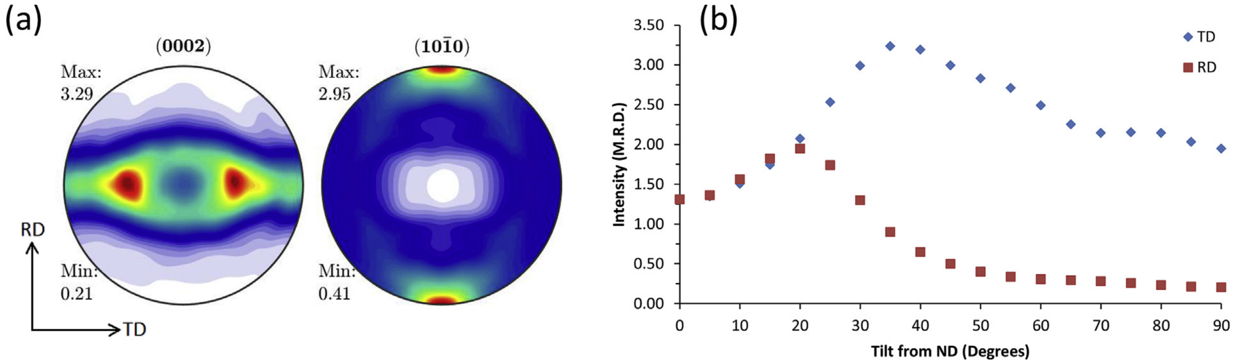


**Fig. 5.** (a) (0002) and (10$\bar{1}$0) pole figure and (b) average intensity (in multiples of random distribution or MRD) from (0002) pole figure as a function of tilt from the normal direction in the rolling (RD) and transverse direction (TD).

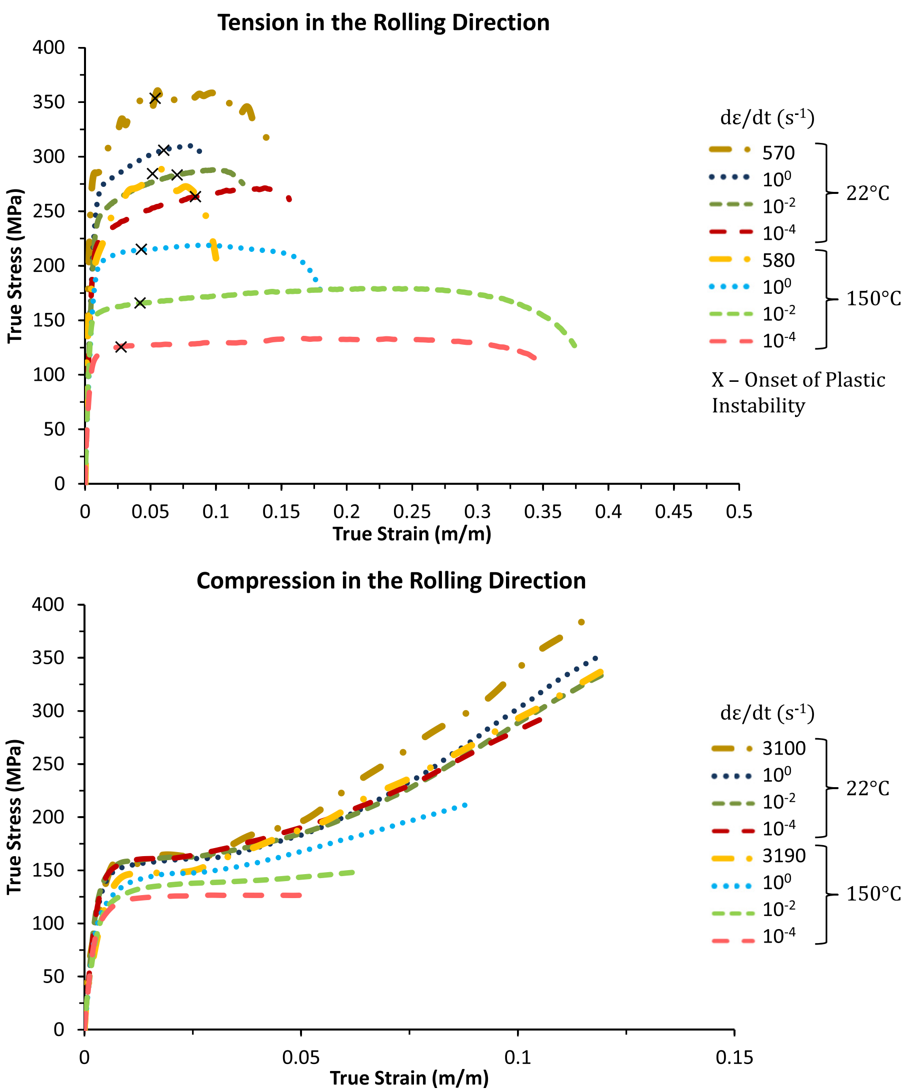


**Fig. 6.** True stress–strain behaviors in tension and compression along the rolling direction at 22 °C and 150 °C and at different strain rates.

hardening exponents at 22 °C for RD, DD and TD are ~0.05–0.07, ~0.13–0.20 and ~0.2–0.25, respectively, which increase as the strain rate increases. The hardening rate at 150 °C decreases compared to that at 22 °C; the strain hardening exponents at

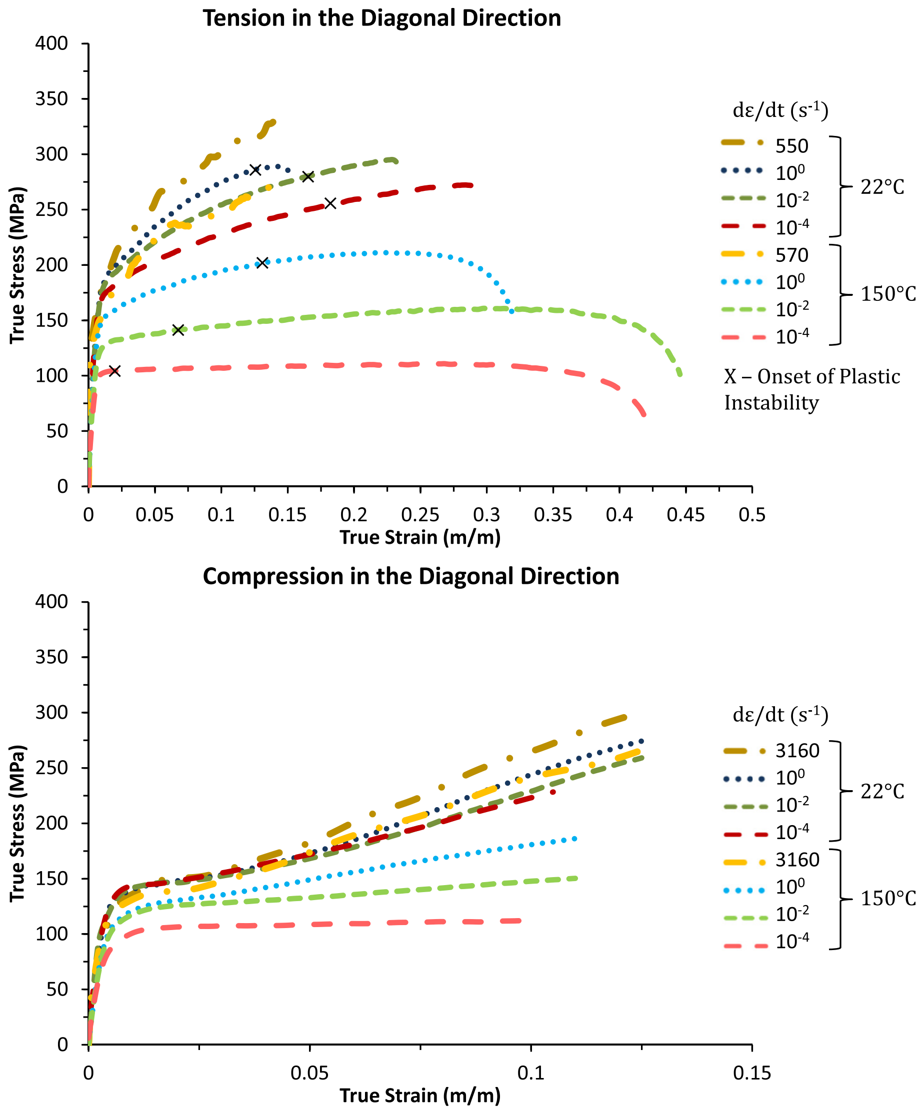


**Fig. 7.** True stress–strain behaviors in tension and compression along the diagonal direction at 22 °C and 150 °C and at different strain rates.

150 °C in the RD, DD and TD are ~0.03–0.09, ~0.05–0.15 and ~0.04–0.18, respectively. Although, the strain hardening exponent fits the data well, the strain hardening at 22 °C in the DD and TD did not follow a typical power law hardening behavior. Similar to Bohlen et al. (2007), there is a greater difference in flow stress between the RD and DD than the TD and DD, where the wide spread of basal poles in the TD governs this behavior. Nonetheless, for tension experiment in the DD, it was observed that the angle between the loading axis and the RD (initially 45°) decreases as the plastic strain increases. The change in angle was macroscopically measured between the rolling residual marks and the loading axis. At 18.2% plastic strain, the angle between the loading axis and the RD decreases to 37° whereas the decrease in angle is approximately linear with plastic strain at the strain rate of $10^{-4}$ $s^{-1}$ and at room temperature. This behavior can be attributed to the significantly different basal pole distribution in the RD and in the TD (Fig. 5) resulting in a rotation of these axes to favor specific deformation mechanisms. The rotation of the textured axes with respect to the loading axis has been shown for other materials such as aluminum and steel (Bunge and Nielsen, 1997; Duchene et al., 2008; Kim and Yin, 1997). This accentuates the importance of plastic spin during plastic deformation and its importance within a modeling framework for magnesium and its alloys (e.g. Han et al., 2002; Lévesque et al., 2010).

The symbols of “x” within tension figures (Figs. 6–8) represent the onset of plastic instability. Necking and facture strains were not measured in tension along the TD and DD at dynamic strain rates due to the time duration and magnitude of the incident wave. Nonetheless, the uniform deformation decreases at 22 °C and increases at 150 °C as the strain rate increases.

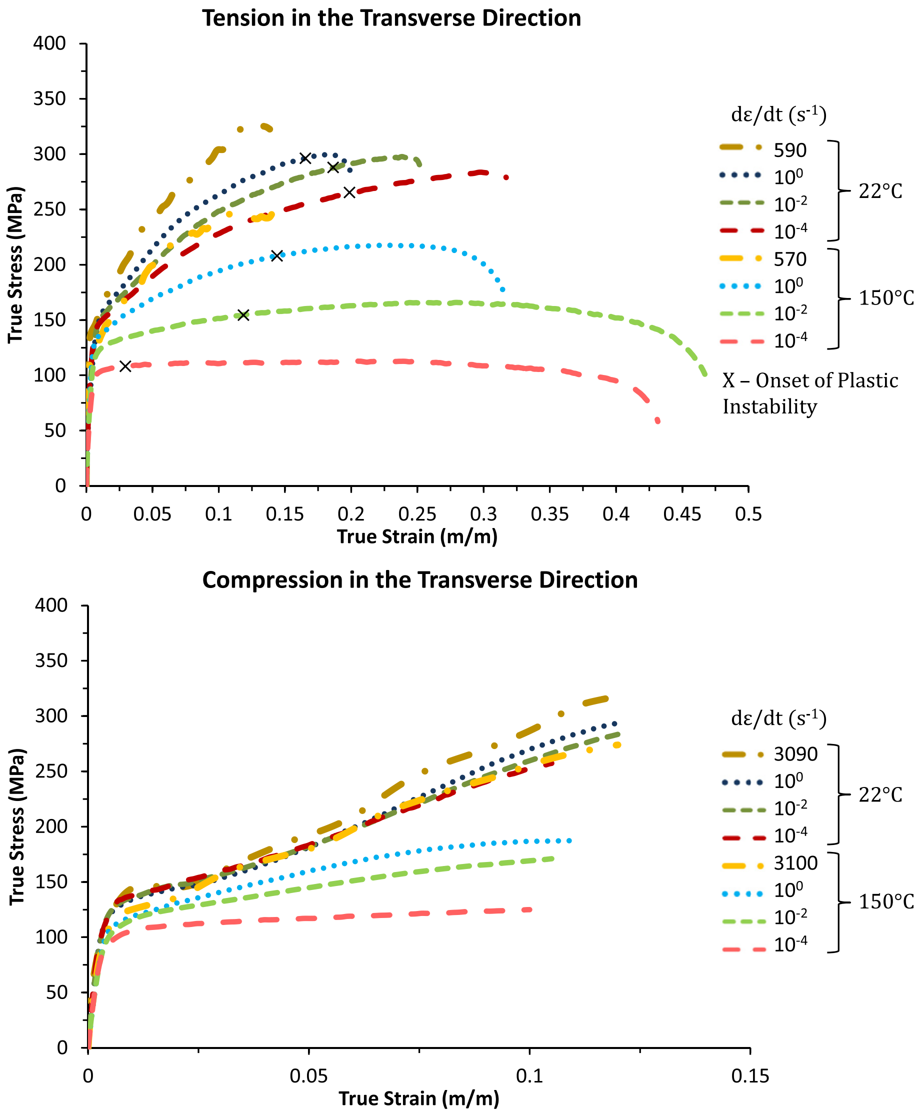


**Fig. 8.** True stress–strain behaviors in tension and compression along the transverse direction at 22 °C and 150 °C and at different strain rates.

While the uniform ductility in the TD and DD are similar, the ductility in the RD is significantly less than in the TD and DD. This behavior can be rationalized by the strain hardening exponent in each direction. As Ghosh (1977) has stated, strain hardening is important in the distribution of strain prior to the onset of diffuse necking. It has been shown that the strain-hardening exponent can be approximated as the strain at the ultimate tensile strength (Dieter, 1986; Hollomon, 1945). Therefore, the lower uniform strain in the RD can be attributed to the low value of strain hardening exponent and thus early unset of tensile instability (Dieter, 1986; Ghosh, 1977). Following uniform elongation, large diffuse necking was observed, followed by localized plastic deformation. At 22 °C, ductility increases as the strain rate decreases. It should be noted, the ductility of ZEK100 was considerably reduced and the samples exhibited sudden fracture from the residual manufacturing rolling marks, specifically in the DD and TD as the strain rate increases. An increase in ductility was observed when the rolling marks and the surface imperfections were removed by light sanding. Similarly on AZ31, Agnew and Duygulu (2005) reported similar sudden fracture on samples with gage length scribes.

Even though plastic instability begins at a relatively small percent plastic strain of ~2–3% at strain rate of $10^{-4}$ $s^{-1}$ and 150 °C, failure strain is 35–45%. It is observed that large diffused necking is favored for increased elongation to fracture. However, at 150 °C, the ductility is the largest at the strain rate of $10^{-2}$ $s^{-1}$. Inherently, an increase in strain rate sensitivity from 22 °C to 150 °C is observed from the stress-strain figures. Therefore, the strain rate sensitivity was modeled using power law and quantified using the following equation:

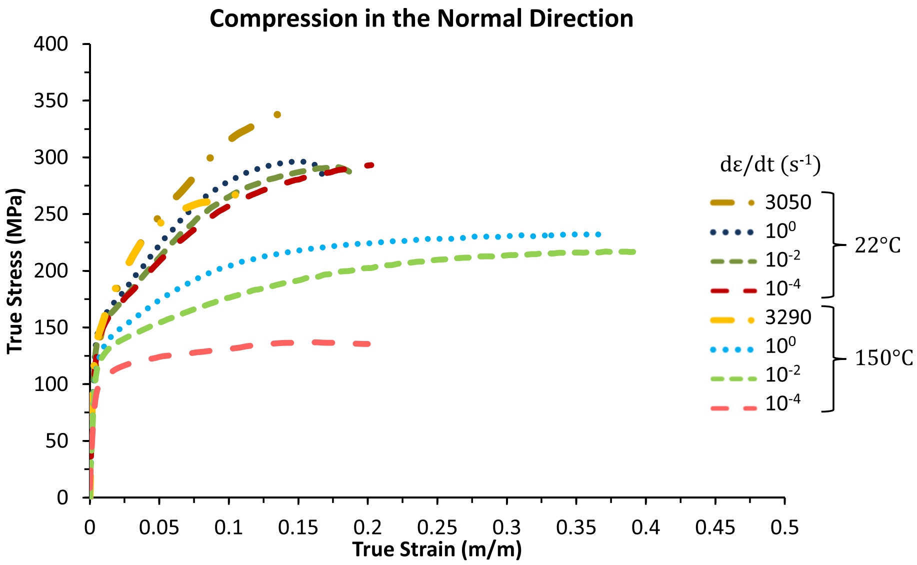


**Fig. 9.** True stress–strain behaviors in compression along the normal direction at 22 °C and 150 °C and at different strain rates.

**Table 2**
Mechanical properties at 22 °C and 150 °C in the rolling (RD), diagonal (DD), transverse (TD) and normal direction (ND).

| | | 22 °C | | | | 150 °C | | | |
|---|---|---|---|---|---|---|---|---|---|
| Direction | Strain Rate ($s^{-1}$) | 0.2% CYS (MPa) | 0.2% TYS (MPa) | Uniform Strain (m/m) | UTS (MPa) | 0.2% CYS (MPa) | 0.2% TYS (MPa) | Uniform Strain (m/m) | UTS (MPa) |
| RD | $10^{-4}$ | 143 | 194 | 0.088 | 242 | 109 | 111 | 0.028 | 122 |
| | $10^{-2}$ | 144 | 213 | 0.073 | 264 | 113 | 148 | 0.043 | 159 |
| | $10^{0}$ | 140 | 240 | 0.062 | 288 | 118 | 191 | 0.044 | 206 |
| | DYN | 145 | 275 | 0.055 | 335 | 129 | 205 | 0.053 | 270 |
| DD | $10^{-4}$ | 128 | 132 | 0.200 | 213 | 84 | 82 | 0.020 | 102 |
| | $10^{-2}$ | 126 | 135 | 0.180 | 237 | 108 | 100 | 0.070 | 132 |
| | $10^{0}$ | 127 | 140 | 0.134 | 252 | 105 | 121 | 0.140 | 177 |
| | DYN | 120 | 151 | – | – | 112 | 143 | – | – |
| TD | $10^{-4}$ | 119 | 120 | 0.220 | 218 | 84 | 86 | 0.030 | 105 |
| | $10^{-2}$ | 120 | 123 | 0.205 | 239 | 102 | 107 | 0.126 | 137 |
| | $10^{0}$ | 118 | 121 | 0.180 | 251 | 109 | 125 | 0.155 | 180 |
| | DYN | 120 | 134 | – | – | 113 | 125 | – | – |
| ND | $10^{-4}$ | 127 | | | | 90 | | | |
| | $10^{-2}$ | 139 | | | | 115 | | | |
| | $10^{0}$ | 140 | | | | 118 | | | |
| | DYN | 135 | | | | 135 | | | |

Note: All values are from engineering stress-strain curves.
CYS, Compressive yield stress; TYS, Tensile yield stress; UTS, Ultimate tensile strength.
DYN: $6x10^2$ $s^{-1}$ for tension; $3x10^3$ $s^{-1}$ for compression.

$$m = \frac{\partial ln\sigma}{\partial ln\dot{\varepsilon}} \tag{8}$$

where m is the strain rate sensitivity parameter evaluated from constant strain rate experiments, σ is the flow stress as a function of true strain, and $\dot{\varepsilon}$ is the strain rate. Ideally, a strain rate jump experiment should be utilized to measure strain rate sensitivity. However, in this case, measurement of strain rate sensitivity using strain rate jump can be erroneous as texture evolution due to mechanical twinning and crystallographic slip is a function of strain and strain rate. For each direction and temperature, separate m values were calculated at different true strain values every 2.5% strain in tension up to the onset of plastic instability. At 150 °C, the strain rate sensitivity parameter calculation at 2.5% true strain includes all strain rates; however, at 5% true strain and thereafter, the strain rate sensitivity parameter calculation excludes the strain rate of $10^{-4}$ $s^{-1}$ due to the onset of plastic instability at ~2.5% true strain. Fig. 10 shows strain rate sensitivity as a function of true strain in

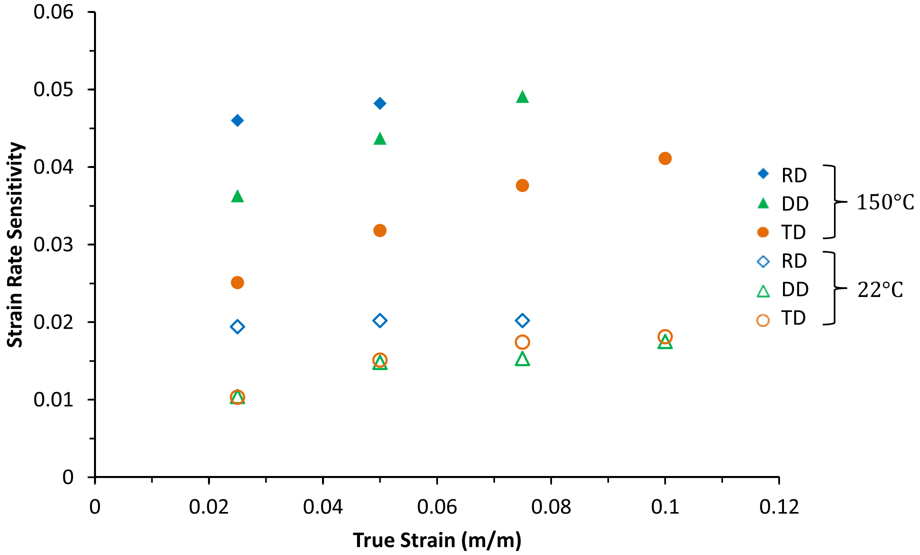


**Fig. 10.** Strain rate sensitivity in tension at 22 °C and 150 °C along the RD, DD and TD.

tension at 22 °C and 150 °C in the RD, DD and TD. In all directions and at all temperatures, positive strain rate sensitivity was observed at all levels of plastic strain. The strain rate sensitivity of ZEK100 is greater at 150 °C than at 22 °C. Ghosh (1977) has pointed out that strain rate sensitivity is an important parameter for diffuse and localized necking. Once the material exhibits post necking deformation, as has been mentioned before, there is an increase in strain rate within the necking region and a commensurate decrease in strain rate outside the necking region. As a result of positive strain rate sensitivity, there is an increase in strength within the necked region, and a decrease in strength outside the necking region. This corresponds to a broad diffused necking region and the delay of the onset of localized necking, and thus large post necking strain (Ghosh, 1977). As mentioned above, diffuse necking was observed at 22 °C, which was amplified at 150 °C. Therefore, the large diffuse necking can be attributed to the increase in work hardening rate as strain rate increases and the increased strain rate sensitivity of the material at elevated temperatures. Nonetheless, at 150 °C, $10^{-2}$ $s^{-1}$ strain rate tends to results in optimum strain hardening and strain rate sensitivity to achieve the maximum percent elongation regardless of direction.

In compression (Figs. 6–9), the yield stress at 22 °C is approximately rate insensitive in all directions (Table 2). It should be noted that all compression experiments in the RD, DD, and TD were interrupted at any sign of failure due to buckling, and therefore, a complete stress-strain curves up to fracture were unattainable. For compressive loading in the ND, stress-strain data at 22 °C was strained to failure, while stress-strain data at 150 °C was stopped after a decrease in stress that might be attributed to thermal softening, barreling and/or the interaction between the sheets. Comparing the yield stress in compression to tension, small to no differences in the TD and DD, and greater difference in the RD (~50–130 MPa) is observed at 22 °C. Compression results in the DD and TD at 150 °C showed a big difference in strain rate sensitivity at yield from strain rate of $10^{-4}$ to $10^{-2}$ $s^{-1}$ and small differences from $10^{-2}$ $s^{-1}$ to dynamic strain rate. In contrast, compression in the RD at 150 °C resulted in a steady but small increase in yield strength as strain rate increases.

In compression, unlike tension, the material shows a sigmoidal hardening indicative of twinning activity in all directions. Sigmoidal hardening was most prominent in the RD, indicating greater activity of twinning. The weaker sigmoid shape hardening in the other direction is a characteristic sign of increased dislocation slip activity. Sigmoid hardening evolution is also more pronounced as strain rate increases at both 22 °C and 150 °C. Moreover, at quasi-static loading and 22 °C, minimum difference is present as the strain rate increases in the RD, DD and TD. However, when comparing quasi-static to dynamic strain rates, an increase in flow stress is observed after 3% strain in the RD, DD and TD. This is not seen for AZ31, where significant strain rate sensitivity was present directly after yielding at dynamic strain rate compared to quasi-static strain rates (Kabirian et al., 2015; Pandey et al., 2015). Similar to ZEK100, Prasad et al. (2014) showed that in case of magnesium alloy ZK60, the flow stress is insensitive to strain rate at small strains when the plastic deformation was mediated by both extension twinning and basal slip. While at larger strains, the flow stress was rate dependent, when comparing quasi-static to dynamics strain rates. Although the study did not focus on any texture based analyses, they attributed the increase in strain hardening to the increase in activity of twinning as the strain rate increases. As described in the following sub-sections, the increase in strain hardening for ZEK100 can be attributed to an increase in strength of the active non-basal slip mechanisms from quasi-static to dynamic loading (Bhattacharyya et al., 2016; Ulacia et al., 2010). Unlike at 22 °C, at 150 °C, positive strain rate sensitivity is present at all plastic strain in all directions. On the other hand, loading in the ND shows a similar high hardening with positive strain rate sensitivity directly after yielding at both 22 °C and 150 °C. Because no buckling occurred during compression loading along the ND, the response up to a larger plastic strain was measured. The flow stress was measured reaching a plateau before fracture at quasi-static strain rates and 22 °C. However, at 150 °C the material reaches a different plateau that increases as strain rate increases. Furthermore, compression in all directions at dynamic strain rates and 150 °C results in similar flow stress to that at quasi-static strain rates and 22 °C.

#### 4.2.2. Anisotropic response

Fig. 11 shows the variation of cumulative r-value for loading along the RD, DD and TD in tension and compression, at both 22 °C and 150 °C, and at strain rates of $10^{-4}$ and $3 \times 10^{3}\ s^{-1}$. The same open symbols at each temperature in tension represent the calculated r-value at four different marked locations within the gage section at a specific strain. Each of the four same symbols corresponds to a different calculated plastic strain where the strains in the width and thickness were used to

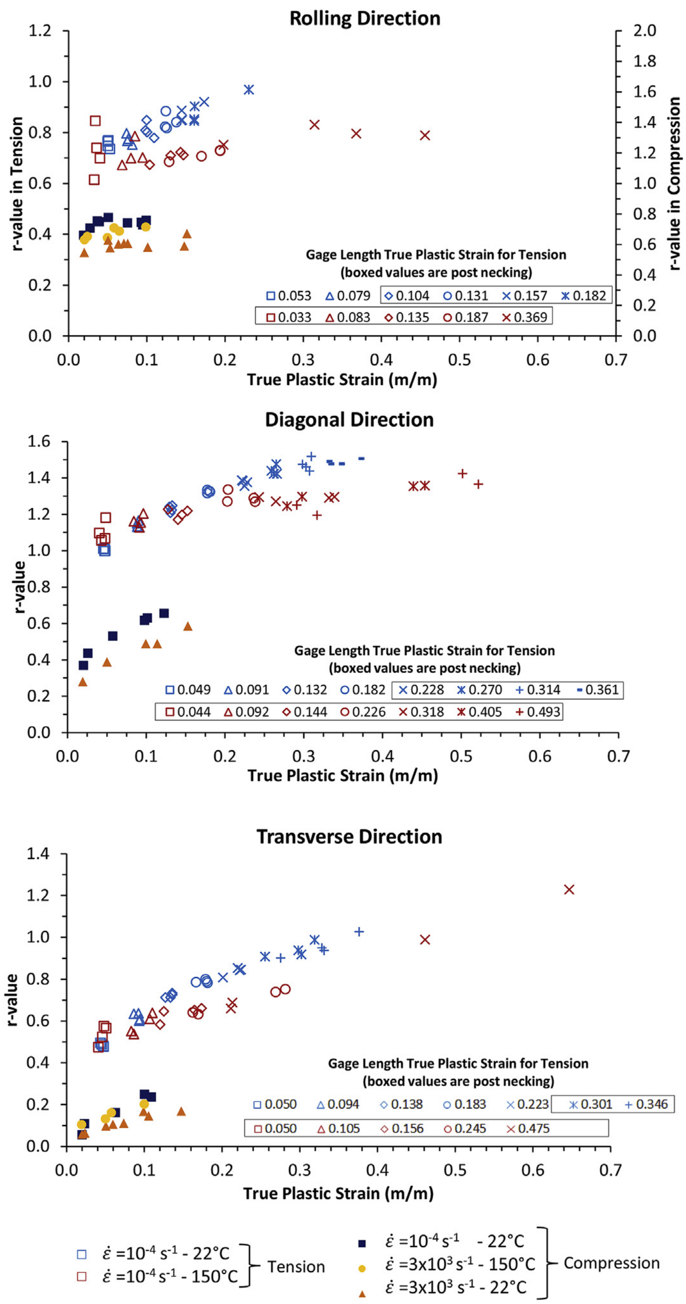


**Fig. 11.** Cumulative r-value as a function of plastic strain for loading along the RD, DD and TD in tension and compression at both 22 °C and 150 °C and at strain rate of $10^{-4}$ and $3 \times 10^{3}\ s^{-1}$; true plastic strain in tension is calculated at a point through incompressibility with a comparison of gage length strain within the subfigures.

calculate the axial strain. Within Fig. 11, the reader can compare the gage length strain to that of the calculated strain at four different marked locations. The measured gage length axial strains are consistent with the calculated axial strain at the four different marked locations up to the onset of plastic instability; the post necking strains and their corresponding r-value are marked within the subfigure.

Consistent with other results on ZEK100 sheets in literature, the r-value increases with increasing plastic strain in both tension and compression (Kurukuri et al., 2014; Muhammad et al., 2015). For loading along the RD, the r-value in tension and compression are similar at the strain rate of $10^{-4}$ $s^{-1}$ and 22 °C even though different deformation mechanisms are active. However, the r-value for the DD and TD in tension and compression show greater differences. The r-value in the DD is greater than 1 in tension unlike the values for loading in the RD and TD. On the other hand, the r-value in compression is the highest in the RD and it decreases as the loading axis is rotated to the TD. At 150 °C in the RD, DD and TD in tension, the r-value at ~5% plastic strain is either greater or the same as the value at 22 °C. At 150 °C and ~5% plastic strain, a large r-value variation throughout the gage length is observed in the RD which was not seen in the DD and TD; this can be associated with the low strain hardening in the RD as mentioned before. Consistent with results on AZ31 sheet, ZEK100 exhibits a decrease in r-value as the temperature increase to 150 °C (Agnew and Duygulu, 2005). Nonetheless, the r-value for compression in all directions decreases as the strain rate increases from $10^{-4}$ to $3 \times 10^3$ $s^{-1}$. As the temperature increases to 150 °C, the r-value at $3 \times 10^3$ $s^{-1}$ increases and it increases to the r-value at $10^{-4}$ $s^{-1}$ and 22 °C. These aforementioned characteristics will be further discussed in section 4.4.4.

Similar to r-value calculations, the relationship between true lateral plastic strain in the TD and RD as a function of true compressive strain in the ND was measured and shown in Fig. 12. The lateral strains in the RD and TD are significantly different for a given axial strain. The relationship between the strain in the TD and the RD is approximately linear for a given axial strain, where the ratio of strain in the TD to the RD is ~2.6.

### 4.3. Texture evolution

#### 4.3.1. Loading along the RD

Deformation by twinning does not only have an impact on the high strain hardening response but also on texture development. When extension twinning is active, tension along the c-axis results in crystal reorientation of ~86° on $\{10\bar{1}2\}$ planes in the $\langle 10\bar{1}1 \rangle$ direction. Extension twinning can result via two separate loading conditions: compression loading perpendicular to c-axis resulting in c-axis extension in the lateral directions, or by direct tension along the c-axis. Even though both conditions cause extension twinning, the texture evolution in each case can be quite different (Hong et al., 2010). Using the initial measured pole figures, it is possible to express qualitatively how the initial grain orientations favor certain deformation mechanisms. During compressive loading, extension twinning will be favorable oriented when the loading direction is perpendicular to the c-axis (Hong et al., 2010). According to the Schmid factor analysis by Nan et al. (2012), for grains to be favorably oriented for non-basal <a> slip, the c-axis of the grains should be oriented 70–90° from the loading axis and a decrease in the Schmid factor as the angle decreases. On the other hand, for pyramidal <c+a> slip to be favorably oriented, the c-axis of the crystal should be oriented 10° and/or 80° from the loading direction to have the highest Schmid factor. For basal <a> slip to be favorably oriented, the c-axis should be 45° from the loading direction; however, as a result of low CRSS of basal <a> slip, crystal orientation deviation of the optimum 45° can results in high activity (Nan et al., 2012). While both non-basal <a> and pyramidal <c+a> might be favorably oriented, their high CRSS, specifically at 22 °C, will hinder their activity in favor for both basal <a> slip and extension twinning (Bohlen et al., 2007; Chapuis and Driver, 2011).

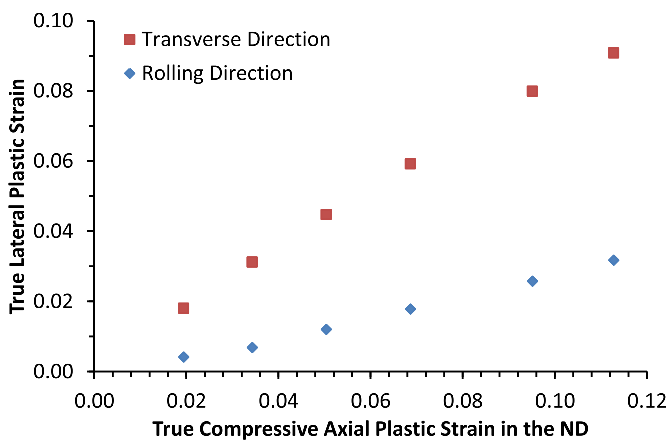


**Fig. 12.** True lateral plastic strain in the transverse and the rolling direction as a function of true compressive strain in the normal direction (ND).

Compression loading along the RD shows orientation preference for extension twinning and non-basal slip (Fig. 5). Even though crystal orientation is not favored for basal <a> slip, as mentioned above, the low CRSS value of basal <a> slip can suggests some activity. Fig. 13 shows the texture evolution of the measured (0002) and $(10\bar{1}0)$ pole figures at the strain rates of $10^{-4}$ and $3 \times 10^3$ $s^{-1}$ at 22 °C and 150 °C along the RD in tension and compression. It can be observed from the pole figures that crystal reorientation is present when the sample is compressed to 2% plastic strain in the RD at the strain rate of $10^{-4}$ $s^{-1}$, signifying high activity of extension twinning in the early stage of deformation. As mentioned in Section 4.2.1, the yield stress in compression along the RD at 22 °C is approximately rate insensitive at all strain rates. Both extension twinning and basal <a> slip have been shown to be approximately rate insensitive by several researchers (Akhtar and Teghtsoonian, 1969a; Brown et al., 2012; Kabirian et al., 2015; Meyers et al., 2001; Ulacia et al., 2010). Therefore, the corresponding initial yield point at 22 °C and at both quasi-static and dynamic strain rates is attributed to both extension twinning and basal <a> slip.

When comparing stress-strain curves at quasi−static and dynamic strain rates, an increase in flow stress is present past 3% strain. Thus, one would expect the (0002) pole intensity in the RD to significantly increase as the strain rate increases from crystal reorientation due to the increase in extension twinning activity at 5% and 10% plastic strain, as shown for AZ31 (Dudamell et al., 2011; Kabirian et al., 2015). However, at 5% plastic strain, the pole figures show minimum differences between the two strain rates. The texture results suggest that relatively similar activity of extension twinning between the two strain rates is present. Interestingly, the initial maximum $(10\bar{1}0)$ intensity oriented in the RD does not translate into $(10\bar{1}0)$ intensity in the ND following crystal reorientation from extension twinning as one would expect (Hong et al., 2010). Initially, the $(10\bar{1}0)$ pole intensity in the RD does not show a 6-fold symmetry radially about the ND due to the wide (0002) pole spread from the ND to the TD. Therefore, after deformation due to extension twinning and lattice spin, the $(10\bar{1}0)$ pole intensity reorients to the TD with poles in a 60° increments and widely spread radially about the loading axis. Similar to 5% plastic strain, at 10% plastic strain, there are minimum differences in the pole figures between the two strain rates. This suggests the increase in flow stress might not be owing to a significant increase in extension twinning activity. The increase in flow stress will be discussed later in Section 4.4.

At the strain rate of $10^{-4}$ $s^{-1}$ and 150 °C, no sign of crystal reorientation is present, signifying approximately no extension twinning activity up to 5% strain, unlike that for extruded AZ31, where significant crystal reorientation is still present at 150 °C

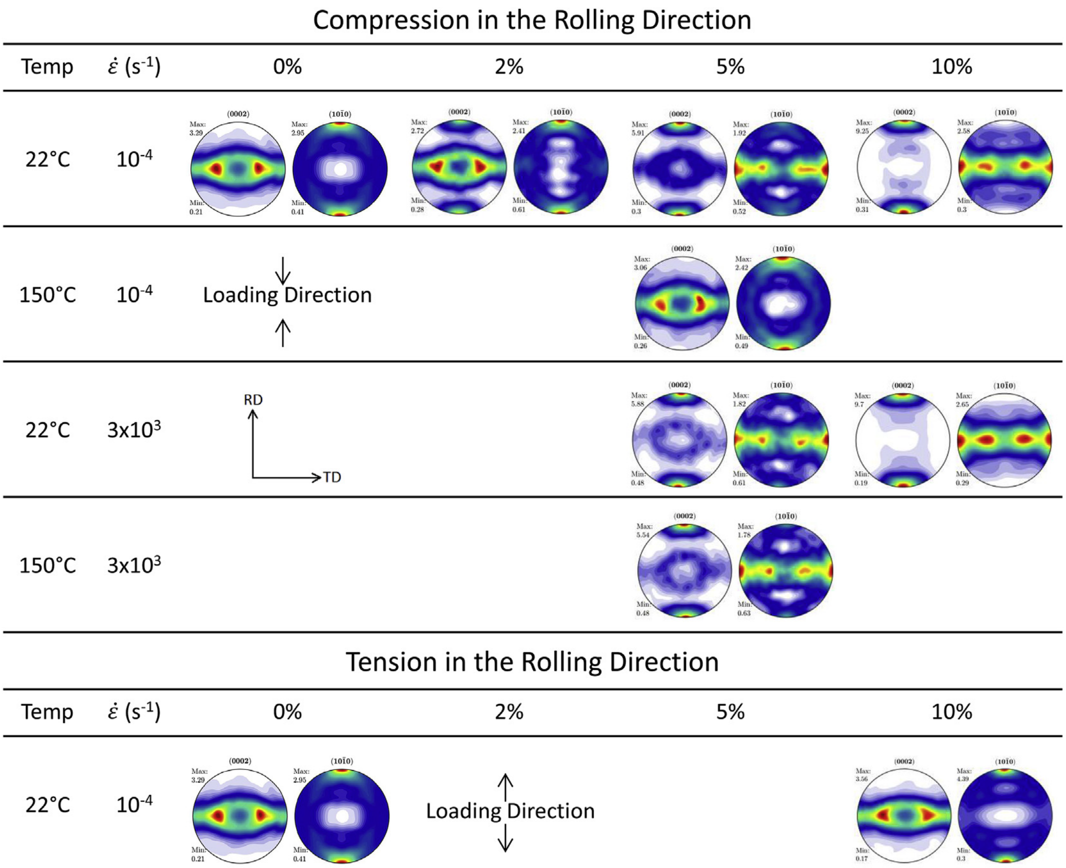


**Fig. 13.** Texture evolution of measured (0002) and $(10\bar{1}0)$ pole figure at strain rates of $10^{-4}$ and $3 \times 10^3$ $s^{-1}$ at 22 °C and 150 °C along the RD in tension and compression.

(Kabirian et al., 2015). The maximum (0002) pole intensity decreases but that can be associated with lattice rotation. This is not to say that no twinning is present, specifically after 5% plastic strain. As mentioned before, experiments at the strain rate of $10^{-4}$ s$^{-1}$ and 150 °C in the RD after 5% plastic strain were unattainable due to buckling of the specimen. Nonetheless, the initial yield stress increases as the strain rate increase from $10^{-4}$ to $3 \times 10^3$ s$^{-1}$ at 150 °C. This can be rationalized by the thermally activated non-basal slip. As the temperature increases, the CRSS of non-basal slip decreases. However, as the strain rate increases, the CRSS of the non-basal slip increases. Hence, at the strain rate of $3 \times 10^3$ s$^{-1}$ and 150 °C at 5% strain, significant crystal reorientation is present, similar to what is observed at 22 °C. This is consistent with the stress-strain data, the flow stress at 150 °C and $3 \times 10^3$ s$^{-1}$ is similar to that at 22 °C and quasi-static strain rates, which suggest similar active deformation mechanisms.

Unlike compression in the RD, the texture pole figures in tension in the RD do not show crystal reorientation from extension twinning. Initially, non-basal slip is favorably oriented in combination with basal <a> slip. At 10% plastic strain in tension along the RD, an increase in intensity for $(10\bar{1}0)$ orientation can be seen. Ulacia et al. (2010) showed that the main deformation mechanism in tension of rolled AZ31 is prismatic <a> slip. This leads to the alignment of $(10\bar{1}0)$ intensity in the tensile direction and a spread of basal pole perpendicular to the tensile axis; a similar trend is observed for ZEK100. The $(10\bar{1}0)$ pole intensity increased in the RD and the spread of (0002) poles became more compact radially around the RD. Therefore, the main deformation mechanism, in addition to basal <a> slip, can be associated with prismatic <a> slip. Even though the $(10\bar{1}0)$ maximum pole intensity is in the RD, the typical 6-fold symmetry is not existent due to the double peaks and the wide spread of (0002) poles in the TD from the ND.

#### 4.3.2. Loading along the TD

In contrast to loading in the RD, loading in the TD contributes to different activities ofslip and extension twinning. Compression along the TD does not favor similar volume of grains oriented for extension twinning as in compression in the RD. The initial grains that favor extension twinning are those whose basal poles are perpendicular to the compressive loading direction, which are all grains with c-axis aligned from the ND to the RD. The initial crystal orientations are also highly oriented for both basal <a> slip, as the loading axis is ±55° from the maximum peak intensity and for non-basal slip due to the wide verity of grain orientation from the loading direction to the ND.

Fig. 14 shows the texture evolution of measured (0002) and $(10\bar{1}0)$ pole figures at the strain rates of $10^{-4}$ and $3 \times 10^3$ s$^{-1}$, at 22 °C and 150 °C along the TD in tension and compression. Crystal reorientation can be observed at 2%, 5% and 10% plastic strains at 22 °C and the strain rate of $10^{-4}$ s$^{-1}$, which is progressive with strain. Even though crystal orientation is highly favored for slip mechanisms, the rate insensitivity of the yield strength at 22 °C and crystal reorientation at 2% plastic strain suggests that the initial yielding is governed by basal <a> slip and extension twinning. Although the compressive yield strength in both the RD and TD are mediated by extension twinning and basal <a> slip, compressive yield strength in the RD is greater than in the TD. The decrease in yield strength in compression along the TD can be attributed to the increased activity of basal <a> slip in the TD.

Comparable to compressive loading in the RD, an increase in flow stress as the strain rate increases is observed after 3% strain. In addition to RD, when comparing the strain rate of $10^{-4}$ to $3 \times 10^3$ s$^{-1}$ at 5% and 10% true plastic strains, similar (0002) pole intensity suggesting similar activity of crystal reorientation. Nonetheless, Hong et al. (2010) showed that loading a crystal along the a-axis can contribute to two different but equal extension twin variants resulting in a crystal reorientation of the c-axis from perpendicular to the loading axis to ±30° from the loading axis towards the orthogonal axis. Similarly, the loading in the TD produced different twin variants that results in (0002) poles that are distributed about the loading axis of ~30°. After deformation, the maximum $(10\bar{1}0)$ pole intensity is still in the RD with majority of the $(10\bar{1}0)$ poles radially around the loading axis. The maximum (0002) pole intensity is located approximately ±10° from the TD towards the ND. As mentioned above, a ±10° basal pole tilt from the loading axis corresponds to highly favorable Schmid orientation for pyramidal <c+a>. A ±10° tilt from the loading axis (TD) to the ND is noticeable at 5% and 10% plastic strain and therefore signifying activity of pyramidal <c+a> slip.

Comparing the stress-strain results and the texture evolution due to extension twinning at 22 °C between RD and TD, it can be assumed that no extension twinning up to 5% strain is present at the strain rate of $10^{-4}$ s$^{-1}$ and 150 °C in compression in the TD. Conversely, when comparing the pole figures at the strain rates of $3 \times 10^3$ s$^{-1}$ at 22 °C and 150 °C, the texture results shows similar amount of crystal reorientation signifying similar activity of extension twinning, similar to compression in the RD.

Furthermore, tension along the TD also favors extension twinning. The grains that are favorably oriented for extension twinning are the grains with the (0002) pole in the TD resulting in direct extension of the c-axis. On the other hand, the active slip mechanisms initially in tension are the same as those in compression. As mentioned above, the initial crystallographic texture is favorable for both basal <a> and non-basal slip. Unlike loading in the RD, essentially no yield tension-compression asymmetry and rate sensitivity are present for loading along the TD at 22 °C (Table 2). Therefore, similar deformation mechanism should be active for both tension and compression in the TD at yield. Thus, the deformation mechanisms that govern the yield strength are both basal <a> slip and extension twinning. At 5% plastic strain, crystal reorientation of the (0002) poles from the TD to radially about the loading axis is observed. This reiterates the activity of extension twinning in the initial phase of plastic deformation. Consequently, grain orientation for non-basal <a> slip increases while still accommodating both basal <a> and pyramidal <c+a> slip systems. At 5% plastic strain, many of the favorably oriented grains for

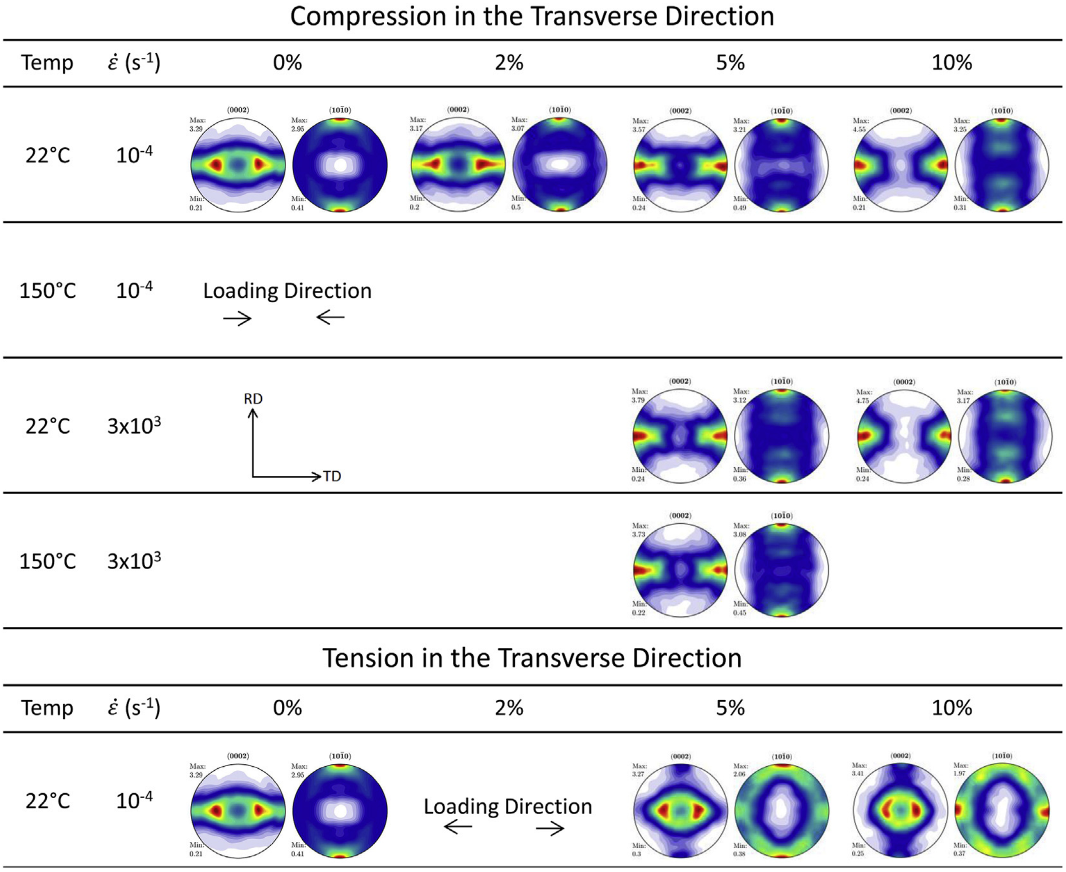


**Fig. 14.** Texture evolution of measured (0002) and ($10\overline{1}0$) pole figure at strain rates of $10^{-4}$ and $3 \times 10^{3}$ s$^{-1}$ at 22 °C and 150 °C along the TD in tension and compression.

extension twinning have undergone crystal reorientation. As plastic strain increases to 10%, additional reorientations of the c-axis of the crystals are present from the TD to radially about the TD, which signifies additional extension twinning activity. Even though the maximum (0002) pole intensity does not increase, this does not indicate that twinning is not accruing; some of the (0002) poles of the twinned crystals reorient to the RD and thus, not contributing to the maximum pole intensity. By 10% plastic strain, the crystal orientations do not favor extension twinning; this is not to say that no twinning is present after 10% plastic strain. It can be seen that after crystal reorientation at 10% strain, the maximum ($10\overline{1}0$) pole intensity is in the TD, which is favorable orientation for prismatic <a> slip. In addition, the wide spread of the basal pole from the ND towards TD (up to ~50°) at 10% plastic strain suggests favorable orientations for both basal <a> and pyramidal <c+a> slips.

### *4.3.3. Compression in the ND*

In the case of compression in the ND, the deformation mechanisms that are favorably oriented are basal and non-basal slips while allowing for deformation by twinning, similar to tension loading in the TD. Initially, the maximum (0002) pole intensity as mentioned above is ~35–40° from the ND to the TD resulting in high activity of basal <a> slip. Fig. 15 shows texture evolution of measured (0002) and ($10\overline{1}0$) pole figures at the strain rates of $10^{-4}$ and $3 \times 10^{3}$ s$^{-1}$ at 22 °C along the ND in compression. The results show crystal reorientation of the (0002) pole from the TD to the ND due to extension twinning as the plastic strain increases at both strain rates. Similar to compression loading in the other directions, the yield strength is rate independent, which can be attributed to rate insensitivity of basal <a> slip and extension twinning. Similar to compression along the RD and TD, minimal difference in the texture evolution between the two different strain rates is present. As the plastic strain increase, there is an increase in the (0002) pole intensities from ~0 to 35° from the ND towards the TD, which represent the grain orientation that is highly favored for a combination of basal <a> and pyramidal <c+a> slip.

## *4.4. Modeling*

The anticipated use of the reduced-order plasticity model (Becker and Lloyd, 2016) is in engineering-scale problems. As such, it sacrifices several mesoscopic crystallographic details unique to magnesium in favor of computational efficiency and robustness. The modeling results of this manuscript are intended to compliment the experimental analysis and to give insight

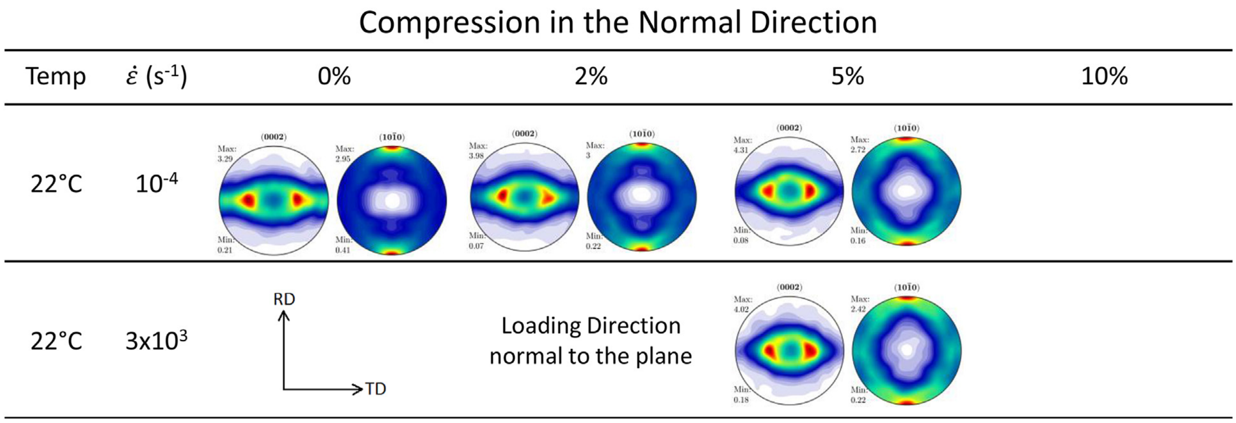


**Fig. 15.** Texture evolution of measured (0002) and (10$\bar{1}$0) pole figure at strain rates of $10^{-4}$ and $3 \times 10^3$ $s^{-1}$ at 22 °C along the ND compression.

in the roles of different deformation mechanism involved in the material behavior. From the data presented in this work, we see negligible dependence of extension twinning on temperature. Although basal <a> slip may have a slight dependence on temperature, it has a much lower CRSS than non-basal slip, and often precedes other deformation modes for all loading cases considered. Therefore, for computational efficiency, we approximate both extension twinning and basal <a> slip as rate-independent and athermal. It is important to reiterate that once Eq. (6) was correlated to the tension loading in the RD to determine material constants, the material parameters in Eq. (6) were unchanged, other than the constant F, during the modeling of basal <a> slip and extension twinning. In addition, a single set of parameters was used to model all the strain rates and temperatures in tension and compression along the RD and TD.

*4.4.1. Stress-strain responses*

Figs. 16 and 17 show the simulated and experimental stress-strain curves at different strain rates and temperatures, in tension and compression, for loading in the RD and TD, respectively. Similar to Meredith et al. (2016), the model was unable to capture the abrupt yield point and perfectly plastic response at low strains in compression at 22 °C when extension twinning and basal <a> slip is the mediated deformation mechanism. However, with reasonable agreement, the model is able to capture the work hardening, anisotropy and tension-compression asymmetry behavior of the material at different strain rates and temperatures in the RD and TD.

*4.4.2. Deformation mechanisms along the RD*

The predicted relative activity of the deformation mechanisms for compression and tension loading in the RD, at different strain rates and temperatures, are shown in Fig. 18. For compression loading in the RD at 22 °C, the model predicts that the initial yield stress and flow stress up to ~5% strain is mediated by both extension twinning and basal <a> slip, hence the low/plateau hardening response after yielding in the stress-strain curves (Fig. 6). Their low CRSS and rate insensitivity reiterates the experimental result of the rate insensitivity of the yield strength in compression (Fig. 6) and the initial crystal reorientation due to extension twinning at 2% plastic strain (Fig. 13). After ~5% strain, the relative activity of extension twinning decreases and the non-basal slip activity increases, while the basal <a> slip activity stays relatively constant. As the strain rate increases from $10^{-4}$ $s^{-1}$ to $3 \times 10^3$ $s^{-1}$, there is an increase in the activity of basal <a> slip and a decrease in the activity of non-basal slip. After the reorientation of the crystal structure within the grains are slowly exhausted from extension twinning, they become favorably oriented for compression along the c-axis. Therefore, the increase in non-basal slip activity as strain increases can be attributed to an increase in the activity of pyramidal <c+a> slip (Dixit et al., 2015). However, unlike the rate insensitivity of basal <a> slip and extension twinning, the CRSS of pyramidal <c+a> slip has been shown to be rate dependent (Bhattacharyya et al., 2016; Ulacia et al., 2010). Consequently, as the strain rate increases, there is a decrease in pyramidal <c+a> slip activity which allows for lower Schmid factor oriented grains for basal <a> slip to increase in activity. Similarly, it has been reported that at high strain rates, long <a> dislocations were observed despite low Schmid factor for basal <a> slip, which they attributed to the low CRSS of basal slip (Dixit et al., 2015).

Comparison of the yield strength of AZ31 sheet (Khan et al., 2011) to the yield strength of ZEK100 in compression along the RD and TD, the yield strength of ZEK100 is greater than that of AZ31, signifying an increase in CRSS of both basal <a> slip and extension twinning. This observation is consistent when comparing the CRSS of basal <a> slip and extension twinning of AZ31 (Ardeljan et al., 2016a; Jain and Agnew, 2007; Kabirian et al., 2015) to what is predicted by the model for ZEK100. Some authors reported that Nd containing Mg-1%Mn alloys exhibited an increase in CRSS of basal <a> slip, compared to conventional magnesium alloys, resulting in enhancement of both twinning and non-basal slip (Dudamell et al., 2013; Herrera-Solaz et al., 2014; Hidalgo-Manrique et al., 2013). This result is consistent with that from the present investigation; based on the modeling results, the CRSS of basal <a> slip is greater than that of extension twinning by 10 MPa. However, Dudamell et al.

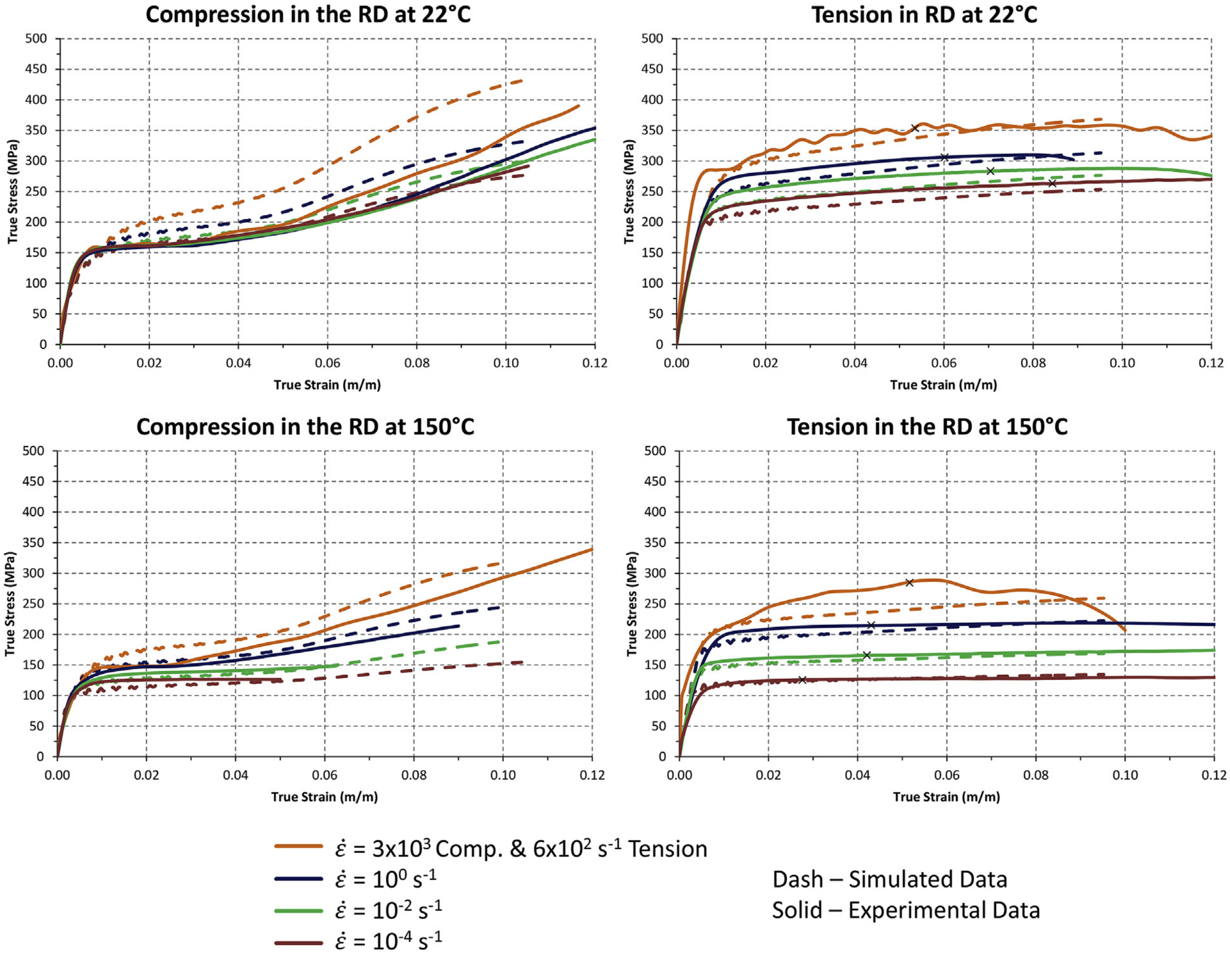


**Fig. 16.** Experimental and simulated true stress–strain behaviors in tension and compression along the RD at 22 °C and 150 °C and different strain rates.

(2013) reported there is a decrease in the CRSS of basal <a> slip as the strain rate increase as the strengthening effect of intermetallic plates on prismatic plane and Nd atoms in solid solution on the basal planes becomes less effective. Similarly, the model suggests that there is an increase in the activity of basal <a> slip at the consequence of the decrease in activity of non-basal slip. Dudamell et al. (2013) also concluded an increase in the basal slip activity and a decrease in extension twinning activity as the CRSS of basal slip decreases. In comparison to Dudamell et al. (2013), Asgari et al. (2014) also observed that the activity of extension twinning decreases with an increase in strain rate. However, they attributed this to the possibility of adiabatic deformation at high strain rates resulting in an increase in the pyramidal <c+a> slip activity. The experimental texture evolution data in this study concludes minimum difference in the extension twinning activity as the strain rate increases. On the contrary, comparing the simulated results performed on magnesium alloy WE43 at low and high strain rates for sample loaded in compression in the RD and TD by Bhattacharyya et al. (2015), their results show a decrease in non-basal slip and a small increase in extension twinning activity at small strains, and an increase in basal <a> slip activity along all strain as the strain rate increases. The decrease in the non-basal slip and the increase in the basal slip are consistent with ZEK100; however, it is difficult to say from the pole figures results for ZEK100, that an increase in extension twinning activity is present at the two different strain rates measured. Nonetheless, the combination of the different constraints of the aforementioned works could have an effect on the approximate indifference of texture evolution at the two opposite strain rates.

As the temperature increases to 150 °C, compression in the RD results in a significant increase in non-basal slip activity at low strain rates, similar to what has been observed by other authors (Akhtar and Teghtsoonian, 1969b; Obara et al., 1973; Raeisinia et al., 2011). Even though the model predicts some activity of extension twinning at 150 °C and $10^{-4}$ $s^{-1}$, no large crystal rotation (~86°) due to extension twinning is observed in the texture evolution pole figure at 5% plastic strain (Fig. 13). As the strain rate increases to $3 \times 10^3$ $s^{-1}$, the non-basal slip activity decreases, while the basal <a> slip activity increases. The influence of the strain rate sensitivity of the CRSS of non-basal slip explains the rate sensitivity of the yield stress at 150 °C. At elevated temperature and low strain rates, dislocation recovery and overcoming thermal barriers, such as

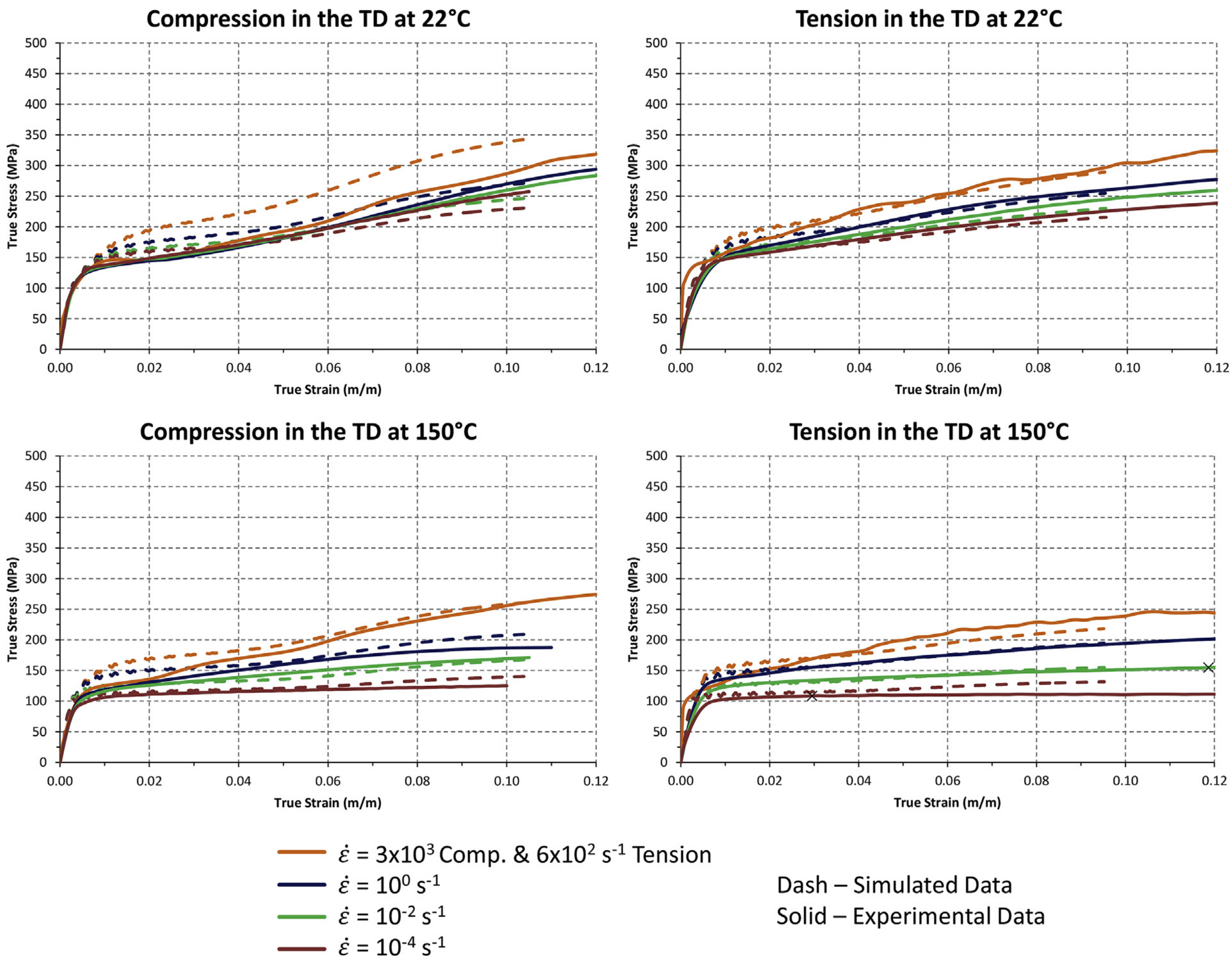


**Fig. 17.** Experimental and simulated true stress–strain behaviors in tension and compression along the TD at 22 °C and 150 °C and different strain rates.

precipitates and solutes, results in an increase in activity of non-basal slip. However, as the stain rate increases to $3 \times 10^3$ s$^{-1}$ at 150 °C, the increase in activity of non-basal slip are reversed and hindered, resulting in similar deformation activity to that at 22 °C. The model was able to predict the similar flow stress and the relative activity of extension twinning at 150 °C and $3 \times 10^3$ s$^{-1}$ to 22 °C and $10^{-4}$ s$^{-1}$.

Unlike compression in the RD, tension in the RD at 22 °C results in a high relative activity of non-basal slip in combination with basal slip. The active deformation mechanism can be attributed to prismatic <a> slip as the CRSS for pyramidal <c+a> slip is typically greater (Bohlen et al., 2007; Ulacia et al., 2010). When the temperature increases to 150 °C, the relative activity of non-basal slip increases and basal <a> slip decreases. Similar to loading in compression, as the strain rate increases, the activity of non-basal slip decreases while the activity of basal <a> slip increases.

#### *4.4.3. Deformation mechanisms along the TD*

The predicted relative activity of the deformation mechanisms for compression and tension loading in the TD, at different strain rates and temperatures, are shown in Fig. 19. The model predicts that the initial yield stress in the TD at 22 °C in compression is due to both the basal slip and extension twinning. An increase in the activity of basal <a> slip and decrease in the activity of extension twinning is observed when comparing the relative deformation activity of the compression loading in the TD to the RD. The initial texture of the material is oriented such that there is a high orientation of grains for basal <a> slip in both compression and tension loading in the TD when compared to the RD. The model was able to predict the increased activity of basal <a> slip in the TD when compared to the RD, and hence the lower yield strength as discussed in Section 4.3.2. Consistent with compression in the RD, the flow stress up to ~5% strain is mediated by basal <a> slip, extension twinning, and then non-basal slip. Also, it can be observed there is an increase in the activity of non-basal slip at higher strains, and an increase in the activity of basal <a> slip at high strain rates. Furthermore, compression in the TD at 150 °C, the model suggests that the relative activity of basal <a> and non-basal slip to be favored at low strain rates. Similarly to compression loading in the RD at 150 °C, as the strain rate increases to $3 \times 10^3$ s$^{-1}$, the non-basal slip activity decreases while the basal <a> slip

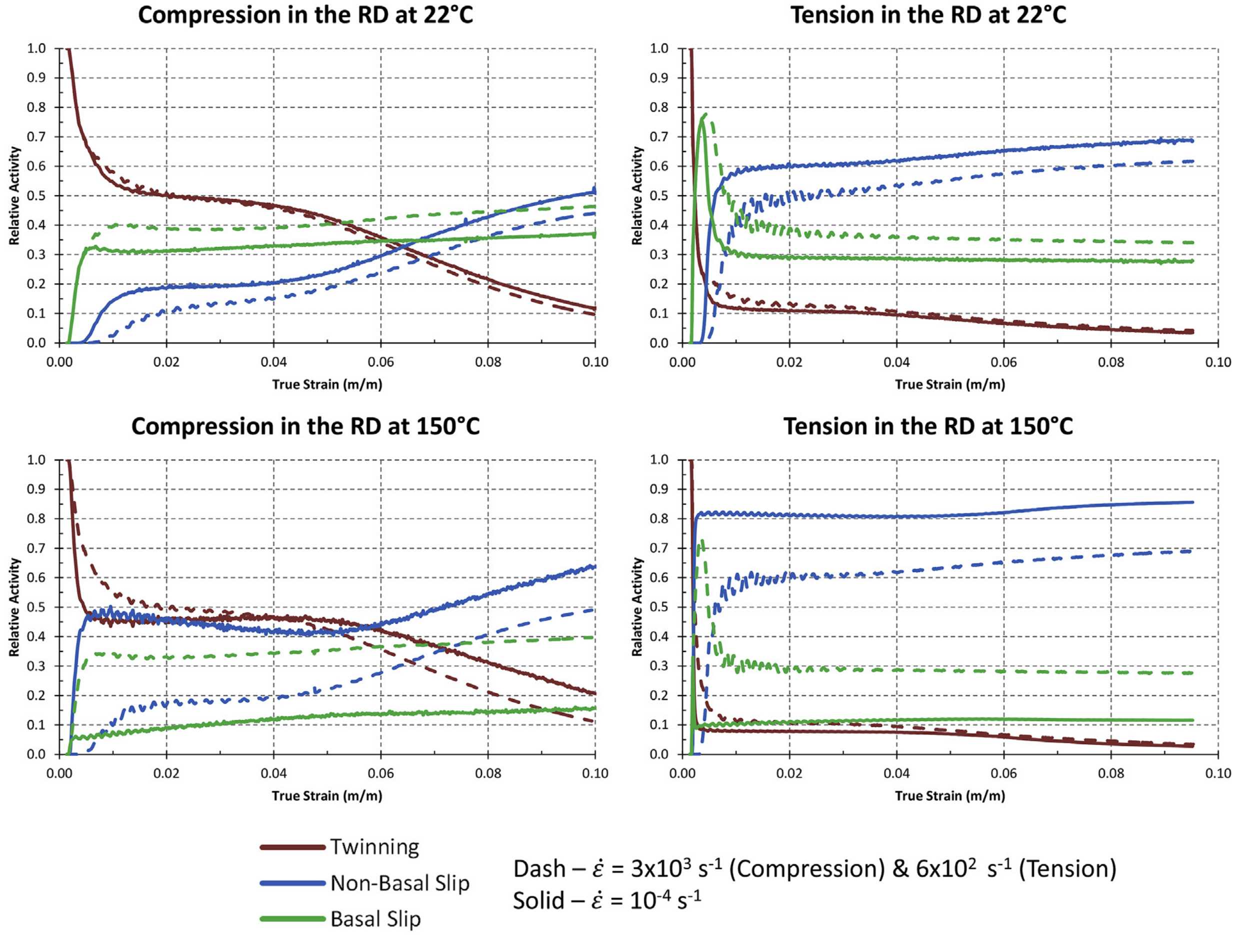


**Fig. 18.** The predicted relative activity of the deformation mechanisms for compression and tension loading in the RD, at different strain rates and temperatures.

activity increases, and the twin activity (up to ~5%) increases. The model was able to predict approximately similar relative activity of extension twinning at the strain rate of $3 \times 10^3$ s$^{-1}$ at 150 °C to that at 22 °C at both strain rates.

As explained in Section 4.3.2, tension loading in the TD, unlike tension in the RD, experiences crystal reorientation due to extension twinning. The model is able to predict the high activity of both extension twinning and basal <a> slip at yielding. On the other hand, as the strain rate increases, the non-basal slip activity decreases and the basal <a> slip activity increases, a similar trend to compression in the TD. As the temperature increases, the model predicts a significant increase in the non-basal slip activity when compared to tension loading at 22 °C, while the basal <a> slip activity decreases.

*4.4.4. Anisotropic response*

As mentioned before, the r-value at the strain rate of $3 \times 10^3$ s$^{-1}$ was observed to be lower than that at $10^{-4}$ s$^{-1}$ in compression. Typically, low r-value in compression is due to extension twinning as a result of initial crystallographic texture, e.g. magnesium alloy AZ31 with initial basal poles in the ND (Jain and Agnew, 2007). Therefore, the decrease in the r-value as the strain rate increases would be a result of the increase in the activity of extension twinning, where the c-axis in the ND reorients to the direction of loading during in-plane compression. However, as seen in the texture evolution Section 4.3 above for ZEK100, minimum texture evolution due to extension twinning is present as the strain rate increases.

Fig. 20 shows the experimental and predicted r-value as a function of strain for loading along the RD and TD in tension and compression at 22 °C and 150 °C and at the strain rate of $10^{-4}$ and $3 \times 10^3$ s$^{-1}$. The predicted modeling results are consistent with the experimental data; the model was able to capture the decrease in the r-value as the strain rate increases in compression. The model predicts that as strain rate increases, there is an increase in the CRSS of non-basal slip and a decrease in its activity while accommodating an increase in the activity of basal <a> slip. Initially, for compression in the RD and TD, the basal pole tilt has the widest spread from the loading axis to the ND. Consequently, there is greater deformation in the thickness direction than in the width from basal <a> slip and hence, a decrease in the r-value as the strain rate increases. Comparatively, the r-value is significantly lower in the TD than in the RD at all strain rates. One reason for this can be due to the greater spread of the basal poles from the TD to the ND, resulting in greater basal <a> slip activity when loading in the TD,

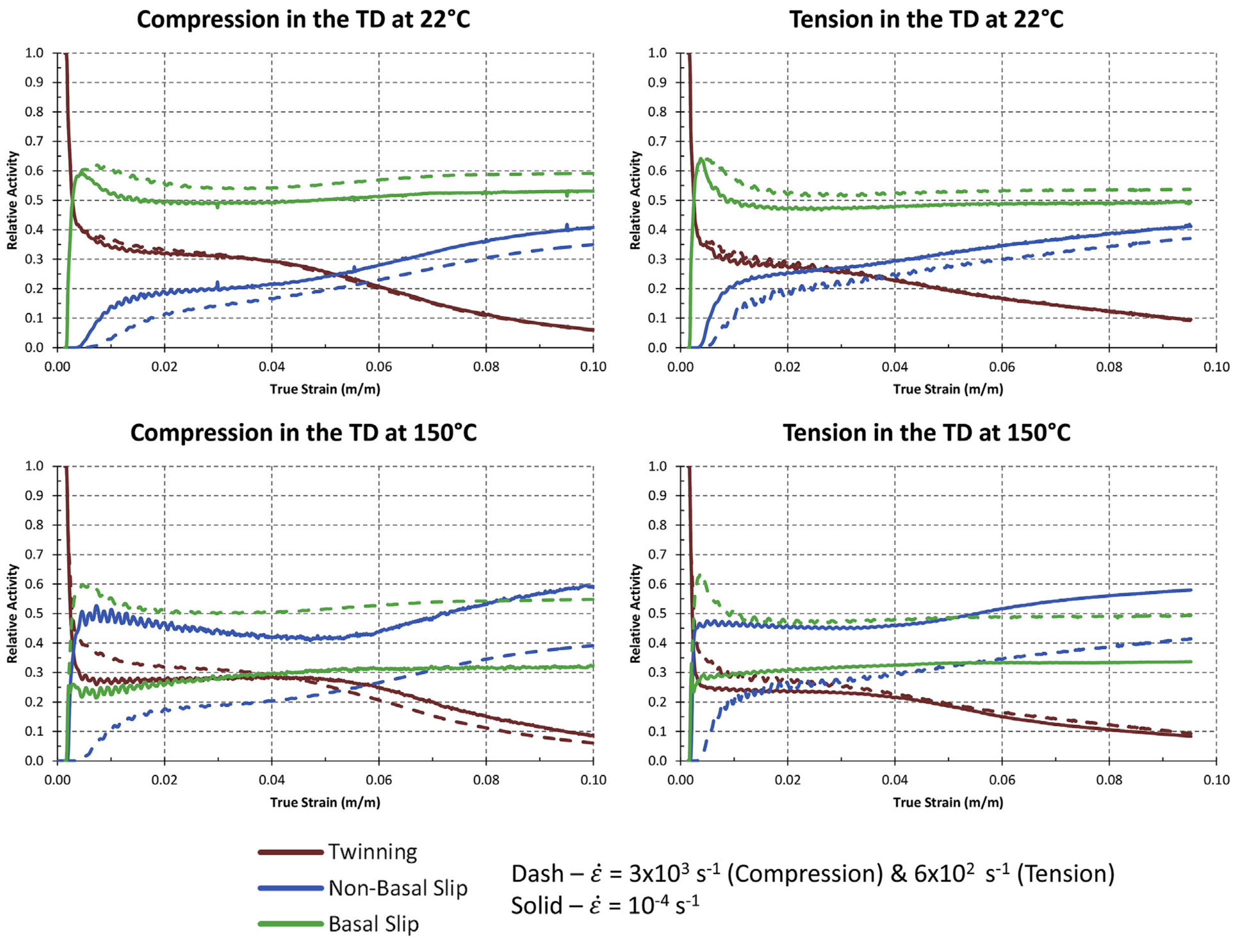


**Fig. 19.** The predicted relative activity of the deformation mechanisms for compression and tension loading in the TD, at different strain rates and temperatures.

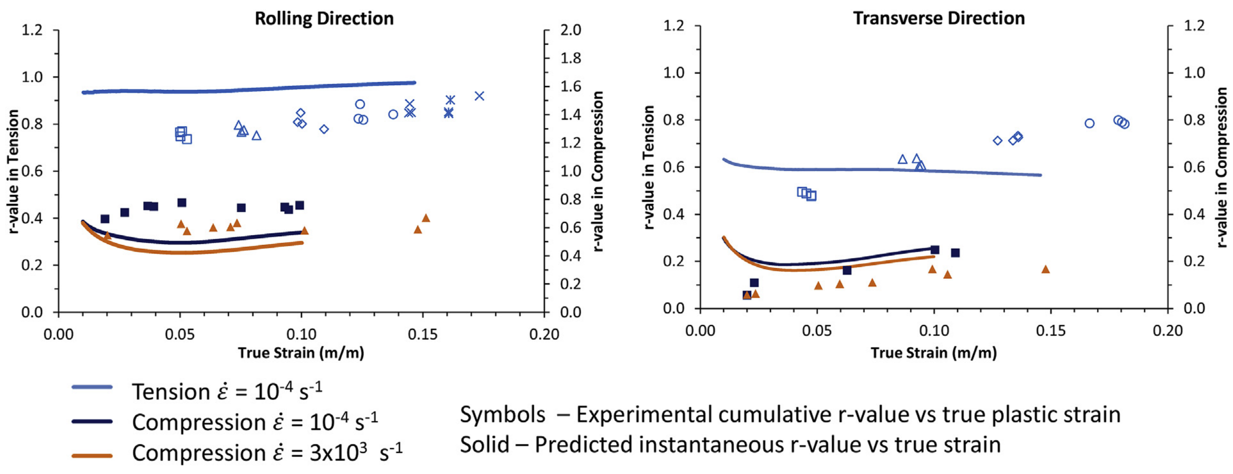


**Fig. 20.** Experimental and predicted r-value as a function of strain for loading along the RD and TD in tension and compression at 22 °C and strain rate of $10^{-4}$ and $3 \times 10^3$ $s^{-1}$.

which allows for greater thickness strain (ND). This comparison is similar to what is seen in magnesium alloy AZ31 sheet at quasi-static strain rates; the r-value is lower for loading in the direction of the maximum basal pole distribution, or loading in the RD (Lou et al., 2007). Another reason for the lower r-value in the TD for ZEK100 is from extension twinning, which is favored for a strain in the through thickness direction. In contrast, for loading in the RD, reorientation of the basal pole from extension twinning is present radially about the loading direction (RD). Nonetheless, comparing the compression r-value results at the strain rate of $3 \times 10^3$ s$^{-1}$ and 150 °C with that at the strain rate of $10^{-4}$ s$^{-1}$ and 22 °C (Fig. 11), the r-value results are similar, in addition to the similar stress-strain curves. Consequently, the expected deformation mechanisms, as mentioned before, are expected to be similar; the model was able to predict similar relative activity of the different deformation mechanisms.

Alternatively, the r-value in tension in the RD and TD correspond to different active deformation mechanisms. For AZ31 (sheet), the main deformation mechanism during in-plane tension is prismatic <a> slip resulting in a maximum prismatic pole in the loading direction with a 6 fold symmetry about the ND after deformation (Atwell et al., 2012; Khan et al., 2011). Analyzing the slip plane and direction, the resulting larger strain is in the width direction and hence the greater than 1 r-value for AZ31. Even though the main contributor to plastic deformation can be attributed to prismatic <a> slip for ZEK100 in tension for loading along the RD, the r-value is less than 1. While the maximum prismatic pole is in the RD, the basal pole tilt is radial about the RD, with a great distribution of basal poles from the TD to the maximum intensity, located ~50° from TD towards ND. As a result, there is more strain in the thickness than the width direction and thus an r-value less than 1. On the other hand, the low r-value in tension in the TD is similar to that in compression in the TD; high activity of basal <a> slip results in a larger strain in the ND and hence the low r-value. In addition, at larger strains, the maximum prismatic poles are in the TD, which represents the characteristic of favoritism of prismatic <a> slip as the strain increases. Consequently, there is an increase in strain in the width direction from prismatic <a> slip and hence the increase in the r-value as the strain increases.

Furthermore, when the material is loaded in compression in the ND, the resulting lateral strains in the RD and TD are different, as shown in Fig. 12. During compression in the ND, grains with the basal pole orientation in the TD exhibit extension of the c-axis and results in crystal reorientation of the c-axis to the ND (direction of loading) due to extension twinning and thus, strain in the TD. In addition to extension twinning, crystal orientation is highly favored for basal <a> and pyramidal <c+a> slips, where the slip direction also cause larger strain in the TD.

## 5. Summary and conclusions

Mechanical response and modeling of magnesium alloy sheet, ZEK100, at quasi-static and dynamic strain rates, at different temperatures and direction of loading were accomplished in this study. The results allow the following conclusions:

- Significant tension-compression asymmetry, specifically in the RD, was present at 22 °C. Increasing the temperature to 150 °C and decreasing the strain rate, reduced the tension-compression asymmetry.
- The difference in yield strength between tension and compression was the largest in RD and diminished with change in orientation to the TD. The yield strength in compression in case of all directions, and tension in the TD and DD at 22 °C were approximately rate insensitive. This was attributed to rate insensitivity of both basal <a> slip and extension twinning. Increasing the temperature to 150 °C resulted in positive strain rate sensitivity at yield due to the increase in the activity of non-basal slip.
- The texture evolution results revealed that compression along all directions resulted in crystal reorientation due to extension twinning. Minimal differences at 22 °C were observed when comparing the pole figures at the strain rate of $10^{-4}$ s$^{-1}$ to the ones at $3 \times 10^3$ s$^{-1}$. While at the strain rate of $10^{-4}$ s$^{-1}$ and 150 °C, there was no discernible crystal reorientation up to the measured 5% plastic strain. Increasing the strain rate to $3 \times 10^3$ s$^{-1}$ at 150 °C resulted in extension twinning activity similar to that at $10^{-4}$ s$^{-1}$ and 22 °C at 5% plastic strain. The model was able to predict relatively constant activity of extension twinning as observed from the experimental results at both strain rates at 22 °C and at the strain rate of $3 \times 10^3$ s$^{-1}$ at 150 °C.
- An increase in compressive flow stress from quasi-static to dynamic loading was observed at 22 °C after 3% plastic strain. According to the results from the model, it was due to the increase in strength of non-basal slip mechanism, which resulted in a decrease in non-basal slip and an increase in the basal <a> slip activity.
- Even though no texture evolution due to extension twinning was observed for tension in the RD, texture evolution due to extension twinning was present for tension in the TD. The results from the model suggested the main deformation mechanisms for tension in the RD are basal and non-basal slip, while tension in the TD was a combination of all deformation mechanisms.
- Variation in the r-value was observed at different strains, strain rates and temperatures. The r-value in tension in the RD and TD was less than the unity at both 22 °C and 150 °C, while the r-value in DD was greater than the unity. Increasing the temperature under tension loading, resulted in a decrease in the r-value. On the other hand, in compression, a decrease in r-value with increase in strain rate was observed, and according to the model, was attributed to an increase in basal <a> slip and a decrease in non-basal slip.

## Disclaimers

Certain commercial firms and trade names are identified in this report in order to specify aspects of the experimental procedure adequately. Such identification is not intended to imply recommendation or endorsement by the National Institute of Standards and Technology, nor is it intended to imply that the materials or equipment identified are necessarily the best available for the purpose.

The findings in this report are not to be construed as an official Department of the Army position unless so designated by other authorized documents. Citation of manufacturer's or trade names does not constitute an official endorsement or approval of the use thereof.

## Acknowledgements

This research was supported in part by an appointment to the Graduate Research Participation Program at the US Army Research Laboratory (ARL) administered by the Oak Ridge Institute for Science and Education through an interagency agreement between the U.S. Department of Energy and ARL. The first author, Saadi Habib, gratefully acknowledges the support from the National Science Foundation Louis Stokes Alliance for Minority Participation Bridge to The Doctorate Fellowship Program (NSF-LSAMP-BD). The authors would like to thank Dr. Raja Mishra of General Motors for supplying the material for this study and Dr. Farhoud Kabirian for his input in the manuscript.

## References

Agnew, S.R., Duygulu, Ö., 2005. Plastic anisotropy and the role of non-basal slip in magnesium alloy AZ31B. Int. J. Plast. 21 (6), 1161–1193.
Agnew, S.R., Tomé, C.N., Brown, D.W., Holden, T.M., Vogel, S.C., 2003. Study of slip mechanisms in a magnesium alloy by neutron diffraction and modeling. Scr. Mater. 48 (8), 1003–1008.
Agnew, S., Whittington, W., Oppedal, A., El Kadiri, H., Shaeffer, M., Ramesh, K.T., Bhattacharyya, J., Delorme, R., Davis, B., 2014. Dynamic behavior of a rare-earth-containing Mg alloy, WE43B-T5, plate with comparison to conventional alloy, AM30-F. JOM 66 (2), 277–290.
Agnew, S.R., Yoo, M.H., Tome, C.N., 2001. Application of texture simulation to understanding mechanical behavior of Mg and solid solution alloys containing Li or Y. Acta Mater. 49 (20), 4277–4289.
Akhtar, A., 1975. Prismatic slip in zirconium single crystals at elevated temperatures. Metall. Trans. A 6 (6), 1217–1222.
Akhtar, A., Teghtsoonian, E., 1969a. Solid solution strengthening of magnesium single crystals—I alloying behaviour in basal slip. Acta Metall. 17 (11), 1339–1349.
Akhtar, A., Teghtsoonian, E., 1969b. Solid solution strengthening of magnesium single crystals—II the effect of solute on the ease of prismatic slip. Acta Metall. 17 (11), 1351–1356.
Al-Samman, T., Li, X., 2011. Sheet texture modification in magnesium-based alloys by selective rare earth alloying. Mater. Sci. Eng. A 528 (10), 3809–3822.
ASTM-E8, 2004. Standard Test Methods for Tension Testing of Metallic Materials. ASTM, West Conshohocken, PA, USA.
Andar, M.O., Kuwabara, T., Steglich, D., 2012. Material modeling of AZ31 Mg sheet considering variation of r-values and asymmetry of the yield locus. Mater. Sci. Eng. A 549, 82–92.
Ardeljan, M., Beyerlein, I.J., McWilliams, B.A., Knezevic, M., 2016a. Strain rate and temperature sensitive multi-level crystal plasticity model for large plastic deformation behavior: application to AZ31 magnesium alloy. Int. J. Plast. 83, 90–109.
Ardeljan, M., Savage, D.J., Kumar, A., Beyerlein, I.J., Knezevic, M., 2016b. The plasticity of highly oriented nano-layered Zr/Nb composites. Acta Mater. 115, 189–203.
Asgari, H., Odeshi, A.G., Szpunar, J.A., 2014. On dynamic deformation behavior of WE43 magnesium alloy sheet under shock loading conditions. Mater. Des. 63, 552–564.
Atwell, D.L., Barnett, M.R., Hutchinson, W.B., 2012. The effect of initial grain size and temperature on the tensile properties of magnesium alloy AZ31 sheet. Mater. Sci. Eng. A 549, 1–6.
Ball, E.A., Prangnell, P.B., 1994. Tensile-compressive yield asymmetries in high strength wrought magnesium alloys. Scr. Metall. Mater. 31 (2), 111–116.
Barnett, M.R., 2007a. Twinning and the ductility of magnesium alloys: Part I."Tension" twins. Mater. Sci. Eng. A 464 (1), 1–7.
Barnett, M.R., 2007b. Twinning and the ductility of magnesium alloys: Part II."Contraction" twins. Mater. Sci. Eng. A 464 (1), 8–16.
Barnett, M.R., Keshavarz, Z., Beer, A.G., Atwell, D., 2004. Influence of grain size on the compressive deformation of wrought Mg–3Al–1Zn. Acta Mater. 52 (17), 5093–5103.
Barnett, M.R., Keshavarz, Z., Beer, A.G., Ma, X., 2008. Non-Schmid behaviour during secondary twinning in a polycrystalline magnesium alloy. Acta Mater. 56 (1), 5–15.
Basu, I., Al-Samman, T., 2014. Triggering rare earth texture modification in magnesium alloys by addition of zinc and zirconium. Acta Mater. 67, 116–133.
Basu, I., Al-Samman, T., 2015. Twin recrystallization mechanisms in magnesium-rare earth alloys. Acta Mater. 96, 111–132.
Basu, I., Al-Samman, T., Gottstein, G., 2013. Shear band-related recrystallization and grain growth in two rolled magnesium-rare earth alloys. Mater. Sci. Eng. A 579, 50–56.
Becker, R., Lloyd, J.T., 2016. A reduced-order crystal model for HCP metals: application to Mg. Mech. Mater. 98, 98–110.
Bhattacharyya, J., Agnew, S., Wu, P., Wittington, W., Kadiri, H.E., 2015. Crystal plasticity modeling of the dynamic behavior of magnesium alloy, WE43-T5, plate. Magnes. Technol. 2015, 165–170.
Bhattacharyya, J.J., Wang, F., Wu, P.D., Whittington, W.R., El Kadiri, H., Agnew, S.R., 2016. Demonstration of alloying, thermal activation, and latent hardening effects on quasi-static and dynamic polycrystal plasticity of Mg alloy, WE43-T5, plate. Int. J. Plast. 81, 123–151.
Boba, M., Butcher, C., Panahi, N., Worswick, M.J., Mishra, R.K., Carter, J.T., 2015. Warm forming limits of rare earth-magnesium alloy ZEK100 sheet. Int. J. Mater. Form. 1–11.
Bohlen, J., Nürnberg, M.R., Senn, J.W., Letzig, D., Agnew, S.R., 2007. The texture and anisotropy of magnesium–zinc–rare earth alloy sheets. Acta Mater. 55 (6), 2101–2112.
Brown, D.W., Beyerlein, I.J., Sisneros, T.A., Clausen, B., Tomé, C.N., 2012. Role of twinning and slip during compressive deformation of beryllium as a function of strain rate. Int. J. Plast. 29, 120–135.
Bunge, H.J., Nielsen, I., 1997. Experimental determination of plastic spin in polycrystalline materials. Int. J. Plast. 13 (5), 435–446.
Chapuis, A., Driver, J.H., 2011. Temperature dependency of slip and twinning in plane strain compressed magnesium single crystals. Acta Mater. 59 (5), 1986–1994.
Chino, Y., Kado, M., Mabuchi, M., 2008. Enhancement of tensile ductility and stretch formability of magnesium by addition of 0.2 wt%(0.035 at%) Ce. Mater. Sci. Eng. A 494 (1), 343–349.
Christian, J.W., Mahajan, S., 1995. Deformation twinning. Prog. Mater. Sci. 39 (1), 1–157.
Dieter, G.E., 1986. Mechanical Metallurgy, third ed. McGraw-hill, Boston, pp. 103–145.
Dixit, N., Xie, K.Y., Hemker, K.J., Ramesh, K.T., 2015. Microstructural evolution of pure magnesium under high strain rate loading. Acta Mater. 87, 56–67.
Drouven, C., Basu, I., Al-Samman, T., Korte-Kerzel, S., 2015. Twinning effects in deformed and annealed magnesium–neodymium alloys. Mater. Sci. Eng. A 647, 91–104.
Duchene, L., Lelotte, T., Flores, P., Bouvier, S., Habraken, A.M., 2008. Rotation of axes for anisotropic metal in FEM simulations. Int. J. Plast. 24 (3), 397–427.

Dudamell, N.V., Hidalgo-Manrique, P., Chakkedath, A., Chen, Z., Boehlert, C.J., Gálvez, F., Gálvez, Yi, S., Bohlen, J., Letzig, D., Pérez-Prado, M.T., 2013. Influence of strain rate on the twin and slip activity of a magnesium alloy containing neodymium. Mater. Sci. Eng. A 583, 220–231.
Dudamell, N.V., Ulacia, I., Gálvez, F., Yi, S., Bohlen, J., Letzig, D., Hurtado, I., Pérez-Prado, M.T., 2011. Twinning and grain subdivision during dynamic deformation of a Mg AZ31 sheet alloy at room temperature. Acta Mater. 59 (18), 6949–6962.
Flynn, P.W., Mote, J., Dorn, J.E., 1961. On the thermally activated mechanism of prismatic slip in magnesium single crystals. Trans. Metall. Soc. AIME 221 (6), 1148–1154.
Ghosh, A.K., 1977. The influence of strain hardening and strain-rate sensitivity on sheet metal forming. J. Eng. Mater. Technol. 99 (3), 264–274.
Groves, G.W., Kelly, A., 1963. Independent slip systems in crystals. Philos. Mag. 8 (89), 877–887.
Hadorn, J.P., Hantzsche, K., Yi, S., Bohlen, J., Letzig, D., Agnew, S.R., 2012. Effects of solute and second-phase particles on the texture of Nd-containing Mg alloys. Metall. Mater. Trans. A 43 (4), 1363–1375.
Hadorn, J.P., Mulay, R.P., Hantzsche, K., Yi, S., Bohlen, J., Letzig, D., Agnew, S.R., 2013. Texture weakening effects in Ce-containing Mg alloys. Metall. Mater. Trans. A 44 (3), 1566–1576.
Han, C.S., Choi, Y., Lee, J.K., Wagoner, R.H., 2002. A FE formulation for elasto-plastic materials with planar anisotropic yield functions and plastic spin. Int. J. Solids Struct. 39 (20), 5123–5141.
Hantzsche, K., Bohlen, J., Wendt, J., Kainer, K.U., Yi, S.B., Letzig, D., 2010. Effect of rare earth additions on microstructure and texture development of magnesium alloy sheets. Scr. Mater. 63 (7), 725–730.
Herrera-Solaz, V., Hidalgo-Manrique, P., Pérez-Prado, M.T., Letzig, D., Llorca, J., Segurado, J., 2014. Effect of rare earth additions on the critical resolved shear stresses of magnesium alloys. Mater. Lett. 128, 199–203.
Hidalgo-Manrique, P., Yi, S.B., Bohlen, J., Letzig, D., Pérez-Prado, M.T., 2013. Effect of Nd additions on extrusion texture development and on slip activity in a Mg-Mn alloy. Metall. Mater. Trans. A 44 (10), 4819–4829.
Hielscher, R., Schaeben, H., 2008. A novel pole figure inversion method: specification of the MTEX algorithm. J. Appl. Crystallogr. 41 (6), 1024–1037.
Hirsch, J., Al-Samman, T., 2013. Superior light metals by texture engineering: optimized aluminum and magnesium alloys for automotive applications. Acta Mater. 61 (3), 818–843.
Hong, S.G., Park, S.H., Lee, C.S., 2010. Role of {10–12} twinning characteristics in the deformation behavior of a polycrystalline magnesium alloy. Acta Mater. 58 (18), 5873–5885.
Hollomon, J.H., 1945. Tensile deformation. Trans. AIME 162, 268–290.
Hosford, W.F., Caddell, R.M., 2011. Metal Forming: Mechanics and Metallurgy. Cambridge University Press.
Huskins, E.L., Cao, B., Ramesh, K.T., 2010. Strengthening mechanisms in an Al–Mg alloy. Mater. Sci. Eng. A 527 (6), 1292–1298.
Jain, A., Agnew, S.R., 2007. Modeling the temperature dependent effect of twinning on the behavior of magnesium alloy AZ31B sheet. Mater. Sci. Eng. A 462 (1), 29–36.
Jain, A., Duygulu, O., Brown, D.W., Tomé, C.N., Agnew, S.R., 2008. Grain size effects on the tensile properties and deformation mechanisms of a magnesium alloy, AZ31B, sheet. Mater. Sci. Eng. A 486 (1), 545–555.
Jiang, L., Jonas, J.J., Mishra, R.K., Luo, A.A., Sachdev, A.K., Godet, S., 2007. Twinning and texture development in two Mg alloys subjected to loading along three different strain paths. Acta Mater. 55 (11), 3899–3910.
Johnson, G.R., Cook, W.H., 1983. A constitutive model and data for metals subjected to large strains, high strain rates and high temperatures. In: Proceedings of the 7th International Symposium on Ballistics, vol. 21, pp. 541–547.
Jones, T.L., DeLorme, R.D., Burkins, M.S., Gooch, W.A., 2007. Ballistic Evaluation of Magnesium Alloy AZ31B. ARL-TR-4077.
Jung, I.H., Sanjari, M., Kim, J., Yue, S., 2015. Role of RE in the deformation and recrystallization of Mg alloy and a new alloy design concept for Mg–RE alloys. Scr. Mater. 102, 1–6.
Kabirian, F., Khan, A.S., Gnäupel-Herlod, T., 2015. Visco-plastic modeling of mechanical responses and texture evolution in extruded AZ31 magnesium alloy for various loading conditions. Int. J. Plast. 68, 1–20.
Kabirian, F., Khan, A.S., Gnäupel-Herlod, T., 2016. Plastic deformation behavior of a thermo-mechanically processed AZ31 magnesium alloy under a wide range of temperature and strain rate. J. Alloy. Compd. 673, 327–335.
Kabirian, F., Khan, A.S., Pandey, A., 2014. Negative to positive strain rate sensitivity in 5xxx series aluminum alloys: experiment and constitutive modeling. Int. J. Plast. 55, 232–246.
Kang, J., Wilkinson, D.S., Mishra, R.K., Yuan, W., Mishra, R.S., 2013. Effect of inhomogeneous deformation on anisotropy of AZ31 magnesium sheet. Mater. Sci. Eng. A 567, 101–109.
Kelley, E.W., Hosford, W., 1968. Plane-strain compression of magnesium and magnesium alloy crystals. Trans. Met. Soc. AIME 242 (1), 5–13.
Khan, A.S., Baig, M., Hamid, S., Zhang, H., 2010. Thermo-mechanical large deformation responses of hydrogenated nitrile butadiene rubber (HNBR): experimental results. Int. J. Solids Struct. 47 (20), 2653–2659.
Khan, A.S., Farrokh, B., 2006. Thermo-mechanical response of nylon 101 under uniaxial and multi-axial loadings: Part I, Experimental results over wide ranges of temperatures and strain rates. Int. J. Plast. 22 (8), 1506–1529.
Khan, A.S., Liang, R., 1999. Behaviors of three B.C.C. metal over a wide range of strain rates and temperatures: experiments and modeling. Int. J. Plast. 15, 1089–1109.
Khan, A.S., Liu, J., Yoon, J.W., Nambori, R., 2015. Strain rate effect of high purity aluminum single crystals: experiments and simulations. Int. J. Plast. 67, 39–52.
Khan, A.S., Pandey, A., Gnäupel-Herold, T., Mishra, R.K., 2011. Mechanical response and texture evolution of AZ31 alloy at large strains for different strain rates and temperatures. Int. J. Plast. 27 (5), 688–706.
Kim, K.H., Yin, J.J., 1997. Evolution of anisotropy under plane stress. J. Mech. Phys. Solids 45 (5), 841–851.
Knezevic, M., Levinson, A., Harris, R., Mishra, R.K., Doherty, R.D., Kalidindi, S.R., 2010. Deformation twinning in AZ31: influence on strain hardening and texture evolution. Acta Mater. 58 (19), 6230–6242.
Knezevic, M., McCabe, R.J., Tomé, C.N., Lebensohn, R.A., Chen, S.R., Cady, C.M., Gray III, G.T., Mihaila, B., 2013. Modeling mechanical response and texture evolution of a-uranium as a function of strain rate and temperature using polycrystal plasticity. Int. J. Plast. 43, 70–84.
Koike, J., Kobayashi, T., Mukai, T., Watanabe, H., Suzuki, M., Maruyama, K., Higashi, K., 2003. The activity of non-basal slip systems and dynamic recovery at room temperature in fine-grained AZ31B magnesium alloys. Acta Mater. 51 (7), 2055–2065.
Kondoh, K., Hamada, E.S.A., Imai, H., Umeda, J., Jones, T., 2010. Microstructures and mechanical responses of powder metallurgy non-combustive magnesium extruded alloy by rapid solidification process in mass production. Mater. Des. 31 (3), 1540–1546.
Kulekci, M.K., 2008. Magnesium and its alloys applications in automotive industry. Int. J. Adv. Manuf. Technol. 39 (9–10), 851–865.
Kurukuri, S., Worswick, M.J., Bardelcik, A., Mishra, R.K., Carter, J.T., 2014. Constitutive behavior of commercial grade ZEK100 magnesium alloy sheet over a wide range of strain rates. Metall. Mater. Trans. A 45 (8), 3321–3337.
Lévesque, J., Inal, K., Neale, K.W., Mishra, R.K., 2010. Numerical modeling of formability of extruded magnesium alloy tubes. Int. J. Plast. 26 (1), 65–83.
Lloyd, J.T., Becker, R., 2016. Stress-based crystal analysis of yielding in rolled Mg AZ31B. Philos. Mag. 96 (4), 370–386.
Lou, X.Y., Li, M., Boger, R.K., Agnew, S.R., Wagoner, R.H., 2007. Hardening evolution of AZ31B Mg sheet. Int. J. Plast. 23 (1), 44–86.
Mackenzie, L.W.F., Pekguleryuz, M.O., 2008. The recrystallization and texture of magnesium–zinc–cerium alloys. Scr. Mater. 59 (6), 665–668.
Meredith, C.S., Khan, A.S., 2012. Texture evolution and anisotropy in the thermo-mechanical response of UFG Ti processed via equal channel angular pressing. Int. J. Plast. 30, 202–217.
Meredith, C.S., Lloyd, J.T., Sano, T., 2016. The quasi-static and dynamic response of fine-grained Mg alloy AMX602: an experimental and computational study. Mater. Sci. Eng. A 673, 73–82.
Meyers, M.A., Vöhringer, O., Lubarda, V.A., 2001. The onset of twinning in metals: a constitutive description. Acta Mater. 49 (19), 4025–4039.

Mishra, R.K., Gupta, A.K., Rao, P.R., Sachdev, A.K., Kumar, A.M., Luo, A.A., 2008. Influence of cerium on the texture and ductility of magnesium extrusions. Scr. Mater. 59 (5), 562–565.
Muhammad, W., Mohammadi, M., Kang, J., Mishra, R.K., Inal, K., 2015. An elasto-plastic constitutive model for evolving asymmetric/anisotropic hardening behavior of AZ31B and ZEK100 magnesium alloy sheets considering monotonic and reverse loading paths. Int. J. Plast. 70, 30–59.
Nan, X.L., Wang, H.Y., Zhang, L., Li, J.B., Jiang, Q.C., 2012. Calculation of Schmid factors in magnesium: analysis of deformation behaviors. Scr. Mater. 67 (5), 443–446.
Nave, M.D., Barnett, M.R., 2004. Microstructures and textures of pure magnesium deformed in plane-strain compression. Scr. Mater. 51 (9), 881–885.
Obara, T., Yoshinga, H., Morozumi, S., 1973. $\{11\bar{2}2\}$< 1123> Slip system in magnesium. Acta Metall. 21 (7), 845–853.
Pandey, A., Kabirian, F., Hwang, J.H., Choi, S.H., Khan, A.S., 2015. Mechanical responses and deformation mechanisms of an AZ31 Mg alloy sheet under dynamic and simple shear deformations. Int. J. Plast. 68, 111–131.
Prasad, K.E., Li, B., Dixit, N., Shaffer, M., Mathaudhu, S.N., Ramesh, K.T., 2014. The dynamic flow and failure behavior of magnesium and magnesium alloys. JOM 66 (2), 291–304.
Raeisinia, B., Agnew, S.R., 2010. Using polycrystal plasticity modeling to determine the effects of grain size and solid solution additions on individual deformation mechanisms in cast Mg alloys. Scr. Mater. 63 (7), 731–736.
Raeisinia, B., Agnew, S.R., Akhtar, A., 2011. Incorporation of solid solution alloying effects into polycrystal modeling of Mg alloys. Metall. Mater. Trans. A 42 (5), 1418–1430.
Ray, A.K., Wilkinson, D.S., 2016. The effect of microstructure on damage and fracture in AZ31B and ZEK100 magnesium alloys. Mater. Sci. Eng. A 658, 33–41.
Rokhlin, L.L., 2003. Magnesium Alloys Containing Rare Earth Metals: Structure and Properties. CRC Press.
Sandlöbes, S., Friák, M., Zaefferer, S., Dick, A., Yi, S., Letzig, D., Pei, Z., Zhu, L.F., Neugebauer, J., Raabe, D., 2012. The relation between ductility and stacking fault energies in Mg and Mg–Y alloys. Acta Mater. 60 (6), 3011–3021.
Sandlöbes, S., Zaefferer, S., Schestakow, I., Yi, S., Gonzalez-Martinez, R., 2011. On the role of non-basal deformation mechanisms for the ductility of Mg and Mg–Y alloys. Acta Mater. 59 (2), 429–439.
Senn, J., Agnew, S.R., 2008. Texture randomization of magnesium alloys containing rare earth elements. Magnes. Technol. 153–158.
Smerd, R., 2005. Constitutive Behavior of Aluminum Alloy Sheet at High Strain Rates (Masters thesis, Waterloo, Canada).
Song, G.L., Atrens, A., 1999. Corrosion mechanisms of magnesium alloys. Adv. Eng. Mater. 1 (1), 11–33.
Staiger, M.P., Pietak, A.M., Huadmai, J., Dias, G., 2006. Magnesium and its alloys as orthopedic biomaterials: a review. Biomaterials 27 (9), 1728–1734.
Staroselsky, A., Anand, L., 2003. A constitutive model for hcp materials deforming by slip and twinning: application to magnesium alloy AZ31B. Int. J. Plast. 19 (10), 1843–1864.
Steglich, D., Tian, X., Bohlen, J., Kuwabara, T., 2014. Mechanical testing of thin sheet magnesium alloys in biaxial tension and uniaxial compression. Exp. Mech. 54 (7), 1247–1258.
Stanford, N., Barnett, M.R., 2008. The origin of "rare earth" texture development in extruded Mg-based alloys and its effect on tensile ductility. Mater. Sci. Eng. A 496 (1), 399–408.
Taylor, G.I., 1938. Plastic strain in metals. Inst. Met. 62, 307–338.
Tenckhoff, E., 2005. Review of deformation mechanisms, texture, and mechanical anisotropy in zirconium and zirconium base alloys. J. ASTM Int. 2 (4), 1–26.
Tucker, M.T., Horstemeyer, M.F., Gullett, P.M., El Kadiri, H., Whittington, W.R., 2009. Anisotropic effects on the strain rate dependence of a wrought magnesium alloy. Scr. Mater. 60 (3), 182–185.
Ulacia, I., Dudamell, N.V., Gálvez, F., Yi, S., Pérez-Prado, M.T., Hurtado, I., 2010. Mechanical behavior and microstructural evolution of a Mg AZ31 sheet at dynamic strain rates. Acta Mater. 58 (8), 2988–2998.
Ulacia, I., Salisbury, C.P., Hurtado, I., Worswick, M.J., 2011. Tensile characterization and constitutive modeling of AZ31B magnesium alloy sheet over wide range of strain rates and temperatures. J. Mater. Process. Technol. 211 (5), 830–839.
Von Mises, R., 1928. Mechanik der plastischen formanderung von kristallen. Z. Angew. Math. Mech. 8, 161–185.
Wang, Y.N., Huang, J.C., 2003. Texture analysis in hexagonal materials. Mater. Chem. Phys. 81 (1), 11–26.
Wendt, J., Kainer, K.U., Arrubarrena, G., Hantzsche, K., Bohlen, J., Letzig, D., 2009. On the Microstructure and Texture Development of Magnesium Alloy ZEK100 during Rolling. In 138th Annual Meeting.
Wonsiewicz, B.C., 1966. Plasticity of Magnesium Crystals. Doctoral dissertation. Massachusetts Institute of Technology.
Yoo, M.H., 1981. Slip, twinning, and fracture in hexagonal close-packed metals. Metall. Trans. A 12 (3), 409–418.
Yoo, M.H., Agnew, S.R., Morris, J.R., Ho, K.M., 2001. Non-basal slip systems in HCP metals and alloys: source mechanisms. Mater. Sci. Eng. A 319, 87–92.
Zerilli, F.J., Armstrong, R.W., 1987. Dislocation-mechanics-based constitutive relations for material dynamics calculations. J. Appl. Phys. 61 (5), 1816–2182.